

Nearby supernova host galaxies from the CALIFA Survey:

II. SN environmental metallicity

L. Galbany^{1,2}, V. Stanishev³, A. M. Mourão³, M. Rodrigues^{4,5}, H. Flores⁵, C. J. Walcher⁶, S. F. Sánchez⁷, R. García-Benito⁸, D. Mast⁹, C. Badenes¹⁰, R. M. González Delgado⁸, C. Kehrig⁸, M. Lyubenova¹¹, R. A. Marino^{12,13}, M. Mollá¹⁴, S. Meidt¹⁵, E. Pérez⁸, G. van de Ven¹⁵, J. M. Vílchez⁸

(Affiliations can be found after the references)

Received December 26th / Accepted —————

ABSTRACT

The metallicity of a supernova progenitor, together with its mass, is one of the main parameters that can rule their outcome. We present the second study of nearby supernova (SN) host galaxies ($0.005 < z < 0.03$) using Integral Field Spectroscopy (IFS) from the CALIFA survey. We analyze the metallicity of 115 galaxies, which hosted 132 SNe within and 10 SNe outside the field-of-view (FoV) of the instrument. Further 18 galaxies, which hosted only SNe outside the FoV were also studied. Using the O3N2 calibrator from Marino et al. (2013) we found no statistically significant differences between the gas-phase metallicities at the locations of the three main SN types – Ia, Ib/c and II, all having $12 + \log(O/H) \approx 8.50$ within 0.02 dex. The total galaxy metallicities are also very similar and we argue that this is because our sample consists only of SNe discovered in massive galaxies ($\log(M/M_\odot) > 10$ dex) by targeted searches. We also found no evidence that the metallicity at the SN location differs from the average metallicity at the galactocentric distance of the SNe. By extending our SN sample with published metallicities at the SN location, we are able to study the metallicity distributions for all SN subtypes split into SN discovered in targeted and untargeted searches. We confirm a bias toward higher host masses and metallicities in the targeted searches. Combining data from targeted and untargeted searches we found a sequence from higher to lower local metallicity: SN Ia, Ic, and II show the highest metallicity, which is significantly higher than SN Ib, Iib, and Ic-BL. Our results support the picture of SN Ib resulting from binary progenitors and, at least part of, SN Ic being the result of single massive stars stripped of their outer layers by metallicity driven winds. We studied several proxies of the local metallicity frequently used in the literature and found that the total host metallicity allows for the estimation of the metallicity at the SN location with an accuracy better than 0.08 dex and very small bias. In addition, weak AGNs that cannot be seen in the total spectrum may weakly bias (by 0.04 dex) the metallicity estimate from the galaxy integrated spectrum.

Key words. Galaxies: general – Galaxies:abundances – (Stars:) supernovae: general

1. Introduction

Heavy elements up to the iron-groups are synthesized by fusion of lighter nuclei in the cores of stars. When the nuclear energy source in the core gets exhausted the star enters the final stage of its life. Within 4–40 Myr after their birth stars heavier than $\sim 8M_\odot$ form a heavy iron core, which gravitationally collapses into a neutron star or a black hole (Bethe et al. 1979; Arnett et al. 1989) triggering explosive ejection star’s outer envelope, an event called core-collapse supernova (CC SN). Stars with masses between 1.5 and $8M_\odot$ form a degenerate carbon-oxygen (C/O) white dwarf (WD) (Becker & Iben 1980) with mass in the range of $0.5 - 1.1M_\odot$ (Dominguez et al. 1999). If a C/O WD is in a binary system, it can accrete mass from the companion star (another WD, a main sequence or red giant star). Under certain conditions the WD can increase its mass to $\sim 1.4M_\odot$ and thermonuclear reactions can ignite in its center to completely disrupt the star in a very bright thermonuclear explosion (Hoyle & Fowler 1960) called Type Ia SN (SN Ia). This general picture is supported by the fact that CC SNe are only found in active star-forming galaxies, spiral arms and H II regions (van Dyk 1992; Anderson et al. 2012; Galbany et al. 2014), which confirms that their progenitors should be massive short-lived stars,

while SNe Ia are found in all types of galaxies, including early type galaxies without ongoing star formation.

The exact understanding of the progenitor systems and explosion mechanism of SNe Ia remains elusive, and no direct progenitor detection has been reported yet (but see McCully et al. 2014). However, there is growing evidence that the progenitor stars of SN Ia have wide range of ages following a delay-time distribution (DTD) with a form close to t^{-1} from hundreds of Myr to 11 Gyr (Maoz et al. 2010). It has been suggested that some small heterogeneities in the observed properties of SNe Ia can be attributed to differences in the mechanism that drives the explosion, such as the nature of the companion star (single or double degenerate scenario) or if the explosion initiates as a detonation or a deflagration.

Type II is the most common class of SN and several progenitor stars have been detected in pre-explosion images, allowing to constrain their initial mass lie between 8.5 to $16.5 M_\odot$ (Van Dyk et al. 2003; Smartt 2015). Although for the peculiar type II SN 1987A a blue supergiant (BSG) was suggested as a progenitor (Hillebrandt et al. 1987), the most viable candidates are red supergiants (RSG, Elias-Rosa et al. 2011; Maund et al. 2011); the more massive ones probably resulting in type IIP (plateau or slow-decliners) and those that have lost large amount of their H envelope and with yellow colors in type IIL (linear, or

Send offprint requests to: lgalbany@das.uchile.cl

fast-decliners). Type II_n SNe show narrow lines in their spectra, which result from interaction between the ejecta and circumstellar matter (CSM). For this reason, it has been proposed that their progenitors could be Luminous Blue Variable (LBV) stars (Smith et al. 2008). Although only a few progenitor detections have been reported (Gal-Yam & Leonard 2009), there is evidence that their progenitors could be less massive than the normal SN II (Anderson et al. 2012; Habergham et al. 2014).

Type Ibc SNe, also called stripped-envelope SNe, are less frequent and less detections are available (See Liu et al. 2015). At the moment of explosion SNe Ic have lost their both H and He layers and thus show no H and He lines in their spectra. SNe Ib have lost only the outer H layer and show He lines. There are two possible channels through which these explosions can occur. In the single-star scenario, the best candidates are massive (>25-30 M_{\odot}) Wolf-Rayet (WR) stars that have been stripped of their envelopes by strong line-driven winds, which are dependent on metallicity (Gaskell et al. 1986; Crowther 2007; Georgy et al. 2009). The other possibility is lower-mass stars that lose their outer envelopes during the evolution in a binary system (Podsiadlowski et al. 1992; Nomoto et al. 1996; Dessart et al. 2011). Although there should be a combination of both scenarios, the binary scenario presently enjoys significant support (Fryer et al. 2007; Smith et al. 2011). A direct progenitor detection in pre-explosion images has been reported, but the exact nature of progenitor system could not be well constrained (iPTF13bvn, Bersten et al. 2014; Eldridge et al. 2015). Finally, SNe Iib are a chameleon class between II and Ib. Initially they show only hydrogen lines in their spectra, but at later stages helium lines also appear. Thus suggests that SN Iib progenitors have retained only a thin layer of hydrogen on the surface. Possible detections of SN Iib progenitor and companion have been reported (1993J, Aldering et al. 1994; Maund et al. 2004; 2011dh, Folatelli et al. 2014; Van Dyk et al. 2014), pointing to red (for 1993J) and yellow (for 2011dh) supergiants as the best candidates.

Given the difficulty of direct progenitor detection even in high-quality pre-explosion images, the characterization of the SN environment has proved to provide constraints on the possible scenarios that lead to different SN type explosions (See Anderson et al. 2015 for a recent review). Among all the parameters that can be measured in the environment, the metallicity is of particular interest, because it is expected to affect many aspects of the SN explosions, including the luminosity of SNe Ia and the type of CC SN produced by the massive stars (Bravo et al. 2010; Moreno-Raya et al. 2016; Modjaz et al. 2011). Most often the observed SN properties have been correlated to global metallicity of their host galaxies either directly measured or inferred from other proxies. Prieto et al. (2008); Kelly & Kirshner (2012); Prantzos & Boissier (2003); Arcavi et al. (2010) all found that the number ratio of SN Ibc to SN II increases with the metallicity. Regarding SNe Ia, Childress et al. (2013) and Pan et al. (2014) found that the Hubble residuals correlated with the host gas-phase metallicity

There are also several examples in the literature that went further and tried to characterize the local properties of the SN environment. This is particularly relevant for the CC SNe, which because of their short-lived progenitors explode closer to their birth place and the metallicity measured at the SN location should be close to that of the progenitor. On contrary, the progenitor stars of SNe Ia most likely lived long enough to migrate around the galaxy, and the host galaxy properties at the SN explosion may not reflect the properties of the progenitor. Modjaz et al. (2008) found that SNe Ic with broad lines, which

are associated with Gamma Ray Bursts, come from significantly lower-metallicity host environments than their counterparts SNe Ic. Using the radial position as a proxy for local metallicity Anderson & James (2009) suggested a similar sequence in the progenitor metallicity of CC SNe. Anderson et al. (2010) and Leloudas et al. (2011) found no statistically significant difference between the local metallicity of SNe Ib and Ic, obtaining slit or fiber spectra at SNe positions. However, Modjaz et al. (2011) used local spectra and central spectra plus a metallicity gradient to claim that larger differences exist between SNe Ic and Ib. Taddia et al. (2013) studied the locations of SN1987A-like events whose progenitors are blue supergiants (BSG), and found lower metallicities compared to other CC SNe subtypes. Also for SNe Ia, several studies tried to measure the local properties of the SN environment either using the offset as a proxy for these local properties (Galbany et al. 2012), or by indirect approximations of the central metallicity and applying decreasing gradients (Boissier & Prantzos 2009).

In this series of papers (Stanishev et al. 2012 and Galbany et al. 2014, hereafter Paper I) we take a different approach. We used wide-field integral field spectroscopy (IFS) at intermediate spectral resolution provided by the CALIFA survey (Sánchez et al. 2012a) combined with other previous observations to measure the properties of the gas and the stellar populations at the location of the SN explosion (in addition to other global host properties). Our goal is to search for differences in environmental parameters among SN types, which would also help to constrain the nature of their progenitors, but we also tested the accuracy of the various proxies to the local metallicity used in the literature. Kuncarayakti et al. (2013a,b, 2015) also used IFS observations, but with a smaller field of view that covered only small part of the galaxies.

In this second paper of the series we focus on the local SN metallicity. The paper is structured as follows. The galaxy sample of SN hosts used in this work is presented in Section 2. The methods used to extract the needed information for this study from the observed IFS data-cubes is outlined in Section 3. We present our results in Section 4. Section 5 contains the discussion of these results, and finally in Section 6 we summarize the conclusions.

2. Galaxy and supernova samples

The galaxy and SN selection is already described in Paper I and more details, including on the data reduction, can be found there. In this work, the sample presented in Paper I was expanded with 33 galaxies (the details are given in Table 1), which hosted 34 discovered SNe. In addition 3 new SNe exploded in two galaxies already presented in Paper I. Thus the total sample used in this work consists of 115 galaxies, with mean redshift of 0.015, that hosted 132 SNe (47 type II, 27 type Ib/c+Iib, 58 Ia) which were in the field-of-view (FoV) of PPAK. 81 galaxies were observed by the CALIFA Survey and 34 from other CALIFA-related studies, using the same instrumental configuration. 12 of the 79 galaxies from CALIFA were delivered to the community in the CALIFA Data Release 1 (DR1, Husemann et al. 2013) and 12 more in the CALIFA DR2 (García-Benito et al. 2015). Table 2 gives the mean and the standard deviation of the redshift distributions of the whole sample and split by SN type.

Seven galaxies from the sample (NGC 214, NGC 309, NGC 628, NGC 1058, NGC 3184, NGC 3913 and NGC 5557) also hosted 10 SNe, which were outside of the FoV of PPAK. Further 18 galaxies from the CALIFA sample have SNe associated with them (one SN in each galaxy), but these SNe are out-

Table 1. Properties of the 37 SNe added to the sample presented in G14. This corresponds to 34 SNe in 33 galaxies observed from June 2014, and 3 SNe that recently exploded in NGC 5404, NGC 6166 and UGC 04132.

Galaxy	Morphology	z	E(B-V)	PA [deg]	b/a	SN	Type	RA offset [arcsec]	DEC offset [arcsec]	Separation [arcsec]
UGC 04132	Sbc	0.017409	0.067	116.7	0.42	2014ee	IIn	-17.1	-14.0	24.9
NGC 5406	SAB(rs)bc	0.017352	0.011	17.9	0.94	PSN J14002117+3854517	II	+5.0	+3.0	4.9
NGC 6166	cD2 pec	0.030354	0.012	123.8	0.95	PS15aot	Ia-91bg	+1.5	-8.6	8.5
NGC 0309	SAB(r)c	0.018886	0.035	26.8	0.93	1999ge	II	+16.0	+6.7	17.6
NGC 0938	E	0.013736	0.100	91.9	0.77	2015ab	Ia	-9.3	+6.3	11.7
NGC 0991	SAB(rs)c	0.005110	0.024	36.7	0.94	1984L	Ib	-32.0	-22.0	35.0
UGC 02134	Sb	0.015297	0.151	8.2	0.51	2011jf	Ibc	+3.0	-1.0	37.2
NGC 1070	Sb	0.013636	0.050	89.8	0.75	2008ie	I Ib	-22.0	+13.0	25.4
MCG -01-09-006 [†]	SB(rs)cd?	0.028977	0.066	107.5	0.32	2005eq	Ia	+15.9	+26.3	30.3
IC 0307 [†]	(R)SB(r)a pec?	0.025981	0.086	149.1	0.61	2005em	I Ib	+38.0	-7.9	38.3
MCG -01-10-019 [†]	SAB(r)cd	0.017505	0.050	105.7	0.72	2001H	II	+5.8	-2.9	4.6
NGC 1667	SAB(r)c	0.015167	0.067	77.8	0.65	1986N	Ia	-12.0	-9.0	19.6
UGC 04195	SB(r)b	0.016305	0.050	111.0	0.71	2000ce	Ia	+15.1	+17.3	22.6
NGC 2554	S0/a	0.013870	0.050	70.0	0.77	2013gq	Ia	-0.6	-9.1	9.2
NGC 2565 [†]	(R')SBbc?	0.011948	0.042	81.1	0.50	1992I	II	-28.5	+7.1	28.9
						1960M	I	-13.0	+34.0	37.6
NGC 2577 [†]	S0	0.00678	0.048	16.8	0.51	2007ax	Ia	-2.6	+5.5	6.4
NGC 2595	SAB(rs)c	0.014443	0.035	125.9	0.95	1999aa	Ia	+1.0	+28.0	30.0
NGC 2596	Sb	0.019807	0.037	158.1	0.40	2003bp	Ib	+17.6	+11.6	22.0
NGC 2604	SB(rs)cd	0.006930	0.041	52.4	0.96	2002ce	II	-16.0	-12.0	23.1
UGC 04468	S0	0.025227	0.030	74.0	0.34	2006bb	Ia	+3.6	-27.5	27.7
NGC 2916	SA(rs)b?	0.012442	0.023	105.8	0.63	1998ar	II	+16.9	+38.5	42.3
UGC 05520	Scd	0.011058	0.034	15.0	0.63	2000L	II	+6.9	-19.3	22.0
NGC 5425 [†]	Sd	0.006918	0.018	38.5	0.35	2011ck	IIP	-14.8	+7.3	16.1
NGC 5525	S0	0.018523	0.022	109.1	0.36	2009gf	Ia	-31.0	-8.5	32.0
NGC 5557 [†]	E1	0.010737	0.006	120.3	0.94	1996aa	Ia	-5.0	+3.0	4.2
NGC 5559 [†]	SBd	0.017232	0.020	152.1	0.33	2001co	Ibc-pec	-13.5	-12.6	18.4
NGC 5587 [†]	S0/a	0.007682	0.023	73.1	0.32	2006dy	Ia	+10.0	+9.0	14.1
NGC 5732	Sbc	0.012502	0.015	130.4	0.56	ASASSN-14jf	II	+8.2	-17.6	20.0
NGC 6063	Scd?	0.00950	0.041	62.5	0.56	1999ac	Ia-pec	+23.9	-29.8	38.3
UGC 10123	Sab	0.012575	0.013	147.5	0.36	2014cv	IIP	+8.0	+2.0	6.0
NGC 7619	E	0.012549	0.072	116.5	0.85	1970J	Ia	-27.0	-30.0	37.0
NGC 7691	SAB(rs)bc	0.013479	0.062	79.1	0.98	2014az	IIP	-22.0	+18.0	28.4
UGC 06517	Sbc	0.008309	0.029	124.2	0.72	2006lv	Ibc	+10.0	+12.0	15.3
IC 0758	SB(rs)cd?	0.004253	0.018	109.8	0.93	1999bg	IIP	-33.0	-20.0	36.6
UGC 09356 [†]	S?	0.007419	0.027	15.2	0.46	2011cj	IIP	+4.4	+7.5	8.2
2MFGC 13321	Sb	0.026145	0.007	168.6	0.39	2002aw	Ia	-1.6	+1.5	3.4

Notes. The morphological galaxy type, redshift, Milky Way dust reddening, and SN angular separation are from the NED database. SN type and offset (positive in the N and E direction) obtained from the Asiago SN catalogue. The position angle (PA, W to N) and the axis ratio (b/a) are calculated in this work. ^(†) Only observed with the V500 grating.

side of the FoV¹. These SNe were only used to check the results of the analysis of the total galaxy properties of the main sample. We always found that adding these extra SNe to the main sample does not change the results. The parameters of these 25 galaxies with SNe outside the FoV are given in Table D.1. In Table 3 the number of SNe in the galaxies in our sample by SN sub-type is summarized.

Almost all SNe in our sample were discovered by targeted searches. It is known that such searches are biased toward more massive galaxies compared to the untargeted ones. As we will see in Sec. 5.1, most galaxies in our sample indeed have masses larger than $\log(M/M_{\odot}) \approx 10$. Thus, the results presented in this work are representative for SNe discovered in targeted searches.

The 3D datacubes used in this work, including those already presented in Paper I, were processed with version 1.5 of the CALIFA reduction pipeline (García-Benito et al. 2015). Nine of the galaxies from Paper I that at the time were observed only with the red V500 grating (spectral resolution $\sim 6\text{\AA}$ and coverage

Table 2. Statistics of the redshift distributions.

	Ia	Ibc/I Ib	II	All
$\langle z \rangle$	0.0179	0.0125	0.0128	0.0150
σ_z	0.0090	0.0063	0.0074	0.0083

	II – Ibc/I Ib	II – Ia	Ibc/I Ib – Ia	CC – Ia
KS test	0.991	0.051	0.063	0.019
($z < 0.02$)	0.951	0.120	0.189	0.087

within 3750- 7300 \AA), have now also been observed with the blue V1200 grating (spectral resolution $\sim 2.7\text{\AA}$ and coverage within 3400- 4750 \AA). For these objects the combined V1200 + V500 datacubes were used.

3. Data analysis

The data analysis has been fully described in Stanishev et al. (2012) and Paper I. Here we just summarize the main steps and add those not included in the previous papers. We note that the measurements presented here and in Paper I are independent

¹ We detected up to twelve supernovae in our galaxy sample that lack from spectroscopic classification. We have not considered them anywhere in this analysis.

Table 3. Statistics of the SNe used in this work. SNe Ia in star-forming (SF) and passive (P) hosts are given separately.

	II	Ibc/I Ib	Ia		All
			SF	P	
SNe in CALIFA hosts	54	32	59	15	160
Inside PPAK FoV	47	27	46	12	132

of the data analysis method used, and a comparison of several methods within the CALIFA collaboration will be matter of a future work (Rosales-Ortega et al. in prep.)

Each galaxy data-cube consists of approximately 4000 spectra spread in square spaxels of $1'' \times 1''$ in a hexagonal field of view (FoV) of 1.3 arcmin^2 . We have applied our analysis procedures to all the individual spectra. For most galaxies the spectra in the outer parts have signal-to-noise (S/N) ratio which is insufficient to extract useful information. To analyze the 2D maps of these galaxies spatial binning was applied using adaptive Voronoi tessellations (Cappellari & Copin 2003; Diehl & Statler 2006). The new combined spaxels were required to have S/N around 20 in the continuum band at $4610 \pm 30 \text{ \AA}$.

The main goal of this paper is to study the metallicity at the SN locations, both stellar and gas-phase. However, in many cases the SN location is on a low S/N spaxel. Because the Voronoi binning is an automatic procedure the new bins are in general not centered at the SN locations. To measure the metallicity at the SN location we followed the same approach as in Paper I. Series of spectra were extracted in apertures centered at the SN positions and with radii up to $6''$. For some SNe even this was not enough to measure the stellar metallicity and a few cases also the gas metallicity². The aperture of the spectrum of each SN used for the analysis in this work is given in Tables D.2 to D.4.

We also analyzed the total galaxy spectra formed by simply summing the individual spaxel spectra with $S/N \geq 1$. This removed the outer low S/N part of the FoV, which contains little light from the galaxy and mostly add noise to the summed spectrum. In several cases, foreground stars in the FoV were also masked out. This analysis was performed in order to compare the properties of the host as derived from integrated spectroscopy, to those derived from spatially resolved spectroscopy.

In order to measure the emission lines flux accurately, the stellar continuum was subtracted using STARLIGHT (Cid Fernandes et al. 2005). We performed series of tests comparing the base of 66 single stellar population (SSP) models with different ages and metallicities from Stanishev et al. (2012) and Paper I, extracted from the Charlot & Bruzual 2007 models (Bruzual 2007), with another basis consisting of 260 SSPs from the basis described in González Delgado et al. (2014). The latter covers ages from 1 Myr to 18 Gyr, four metallicities – 0.2, 0.4, 1.0 and $1.66 Z_{\odot}$, where $Z_{\odot} = 0.019$, and uses Salpeter (1955) initial mass function (IMF). We found that which basis is used has little effect on the measured emission line fluxes. Thus, to speed up the analysis the 66 SSPs basis was used for the continuum subtraction and measurement of the gas-phase properties. The most prominent emission lines were fitted using a weighted non-linear least-square fit with a single Gaussian plus a linear term, and corrected for dust attenuation using the ratio of $H\alpha$ and $H\beta$ emission line fluxes. Finally, spatially resolved 2D maps of the flux and error for each line were produced.

² Even though metallicity is derived from the spectra at the SN spaxel with $1 \times 1''$ size, the resolution of the cubes is $\sim 2.57''$. The effect of this will be further discussed in Sec 5.2.

For the analysis of the properties of the stellar populations, our test indicated that the properties recovered with the larger basis were more stable and in particular in a given galaxy the stellar metallicity showed smaller scatter. Thus, the estimations of the stellar mass from the total spectra, and the stellar age and metallicity for each particular measurement, were obtained from the STARLIGHT fits with the 260 SSPs basis. In this work we focus only on the mass-weighted metallicity estimate. For calculating the galaxy masses, the distances inferred from Hubble law were used. Only for the very nearby galaxies distances from Cepheid, Tully-Fisher or other direct methods were used when available.

3.1. Oxygen abundance

Nebular emission lines are a good tracer of the young and massive stellar populations that ionize the interstellar medium (ISM), and are the main tool at our disposal for the direct measurement of the metal abundance. Since oxygen is the most abundant metal in the gas phase and exhibits very strong nebular lines in optical wavelengths, it is usually chosen as a metallicity indicator in ISM studies. The most accurate method to measure ISM abundances (the so-called direct method) involves determining the ionized gas electron temperature, T_e , which is usually estimated from the flux ratios of auroral to nebular emission lines (e.g. $[\text{O III}] \lambda\lambda 4959, 5007 / [\text{O III}] \lambda 4363$, Izotov et al. 2006; Stasińska 2006). However, the temperature-sensitive lines such as $[\text{O III}] \lambda 4363$ are very weak and difficult to measure, especially in metal-rich environments. Using V1200 CALIFA data for 150 galaxies, Marino et al. (2013) (M13 hereafter) identified only 16 H II regions from which this line can be measured and used them to reliably derive T_e . Due to the difficulty to find the needed emission lines to estimate the metallicity using the direct method, other alternatives have been developed over the years. The so-called empirical methods consist of a combination of easily measurable gas emission parameters that are calibrated against the metallicities previously determined by the direct method from H II regions and galaxies. Instead, the theoretical methods are calibrated by comparing the measured line fluxes with those predicted by theoretical photoionization models. While these two methods have been probed to be sensitive to relative variations of the metallicity, they also showed systematic differences on the absolute metallicity scale (see Kewley & Ellison 2008 for a review). Indeed, the theoretical methods have been showed to overestimate the metallicity by a few tenths of dex, and the empirical methods may underestimate it (Moustakas et al. 2010). Since our aim is to determine the gas oxygen abundances at SN sites within the galaxies, and the direct method cannot be used everywhere reliably with our data, we used several alternative methods described above.

As a primary method, we use the empirical calibration based on the O3N2 index, firstly introduced by Alloin et al. (1979), which gives an estimation of the oxygen abundance from the difference of the O3 and N2 line ratios. This calibration has the advantage (over other methods) of being insensitive to extinction due to the small separation in wavelength of the emission lines used for the ratio diagnostics and not suffer from differential atmospheric refraction (DAR). Anyway, the extinction is not a problem in our case since our emission lines measurements are already extinction corrected. Recently, M13 presented new calibrations for this O3N2 and for the N2 indices including new direct abundance measurements at the high metallicity regime, which is an advantage compared to the mostly used Pettini & Pagel 2004 (hereafter PP04) O3N2 calibration

that used instead photoionization models for that regime. Although the relative differences between the two calibrations are kept, these new calibrations give more physical results, not allowing for example very high values of the oxygen abundance (e.g. >9.0 dex). For this reason, the main analysis will be done using the empirical calibration introduced in M13.

We used three alternative methods to check the O3N2 results: (a) the M13 calibration based only on the N2 index; (b) the method described in Pilyugin et al. 2010 (hereafter P10) which makes use of the [O II] $\lambda\lambda 3726,3729$ doublet; and (c) the method described in Pilyugin & Mattsson 2011 (hereafter P11) that uses the [S II] doublet.

We note that those emission lines measurements that fall in the AGN region in the BPT diagram (Baldwin et al. 1981) according to the Kewley et al. (2001) criterion, were excluded from the analysis everywhere in the paper. This happened basically in the central spaxels of a significant fraction ($\sim 50\%$) of our galaxies.

3.2. Metallicity gradients

The radial variation of the metal abundance in galaxies has been studied in several works using a wide range of approaches and instruments (Diaz 1989; Zaritsky et al. 1994; Garnett et al. 1997; Henry & Worthey 1999; Rolleston et al. 2000; Boissier & Prantzos 2009; Sánchez et al. 2012b; Marino et al. 2016). The existence of radial metallicity decrease towards the galaxy outskirts is now commonly accepted and it can be explained by the combined effects of a radially varying star formation rate and gas in-fall. It has also been suggested in the past that the magnitude of the radial decrease has a characteristic value (Diaz 1989; Vila-Costas & Edmunds 1992; Bresolin et al. 2009; Yoachim et al. 2010; Rosales-Ortega et al. 2011). IFS is the technique best suited to study in detail the metal abundance distribution across the galaxy surface and gain insight on its radial dependence. Using HII regions of about 300 galaxies observed by CALIFA Sánchez et al. (2014) have demonstrated the universality of the gradient, which has been confirmed by Sánchez-Menguiano et al. (2016) performing a spaxel by spaxel analysis.

We determined metallicity gradients in our galaxy sample using our methodology to estimate the disk effective radius (see Appendix A), and the galaxy position angle and inclination. For each galaxy the metallicity obtained at each spaxel was plotted as a function of the deprojected galactocentric distance and fitted with a first-order polynomial to estimate the galaxy metallicity gradient. As stated in Section 3.1, the central spaxels showing emission coming from AGN were removed from the fit because the gas emission lines observed in such regions are not due to ionization coming from young massive stars. All the 11 passive/elliptical galaxies in our sample show weak emission in their central regions, which in all cases was classified as coming from an AGN. Five of these galaxies also showed traces of weak emission lines in the central parts outside the AGN-affected region, but those were not strong enough for measuring gradients.

Generally, in most galaxies the metallicity decreases with the radial distance. A clear example of the general case is given in Figure 1 (top panel) for NGC 4961. However, in some galaxies a metallicity decrease or flattening close to the center was found (see UGC 03555 in Fig. 1 bottom panel). This central metallicity decrease was first noted by Rosales-Ortega et al. (2011) and Sánchez et al. (2012b), and was studied in more detail with the whole CALIFA sample by Sánchez et al. (2014), who found that about 25% of the galaxies showed it. This feature appears to

be associated with a circumnuclear star-formation ring, where gas tends to accumulate due to non-circular motions (Fathi et al. 2007), and does not seem to be associated with the morphological type of galaxies or with the presence of a bar. In our sample, 18 out of 58 (31%) of the SN Ia, 13 out of 47 (28%) of the SN II, and 7 out of 27 (26%) of the SN Ibc host galaxies showed the central decrease. If we include those galaxies that show a flattening rather than a decrease toward the center, all percentages would increase to around 40%. It is also interesting to note that $\sim 50\%$ of the galaxies hosting an AGN (27 out of 58) show the central metallicity decrease and excluding the 11 elliptical galaxies the percent increases to $\sim 60\%$ (27 out of 47). Besides, 30% (8 out of 27) of the galaxies that fall in the composite region of the BPT diagram also show the decrease, but only one located in the star-forming region (UGC 03555) shows this effect. Exploring the possible connection between the central metallicity decrease and the presence of AGN is certainly interesting, but it is beyond the scope of this paper.

4. Results

In this section we explore the 2D maps of SN host galaxies in search for correlations between the SN type and the properties of their host galaxies regarding the gas elemental abundance and the stellar metallicity. There are 11 galaxies (host of 12 SNe Ia) in our sample which after subtracting the stellar continuum contribution, do not show emission lines at any position or only show weak emission in their central regions: NGC 0495, NGC 1060, NGC 2577, UGC 04468, NGC 4874, NGC 5557, NGC 5611, UGC 10097, NGC 6166, NGC 6173, and NGC 7619. As in Paper I, we use these 12 SNe Ia only when the parameter needed for the analysis is measurable. In the following sections most of the results are presented in the form of cumulative distributions (CDFs). We have performed tests to check whether the differences between the mean values and the standard deviations of the distributions are statistically significant. Two-sample Kolmogorov-Smirnov (KS) tests were also performed to check whether the data was drawn from the same underlying population. The measured quantities for individual galaxies/SNe are reported in Tables D.2, D.3, and D.4. In Tables 4-7 we give the mean and median statistics of the distributions and their asymmetric errors for the three SN subtypes.

4.1. Global and local metallicities

The cumulative distributions of the local gas and stellar metallicities for each SN type are shown in the upper row of Fig. 2, and the properties of the distributions are given in Table 4. There are differences between the distributions of the local gas-phase metallicity among the SN types, but the KS test indicates that only the distribution of SN Ia and SN II could be different at 95% significance. The differences between the mean total metallicities are also small (~ 0.04 dex) and the statistical tests again indicate that the differences could be significant only between SN Ia and SN II at 95% significance. It is also interesting that the standard deviation of the distribution for SNe Ia is twice smaller than those of the core-collapse SNe, and this difference appears to be statistically significant. The differences between the mean stellar metallicity at the SN location are larger than for the gas-phase metallicity, but the standard deviations of the distributions are also significantly larger. The KS test indicates no statistically significant differences between the distributions. Even though the differences between the mean metallicities at the SN loca-

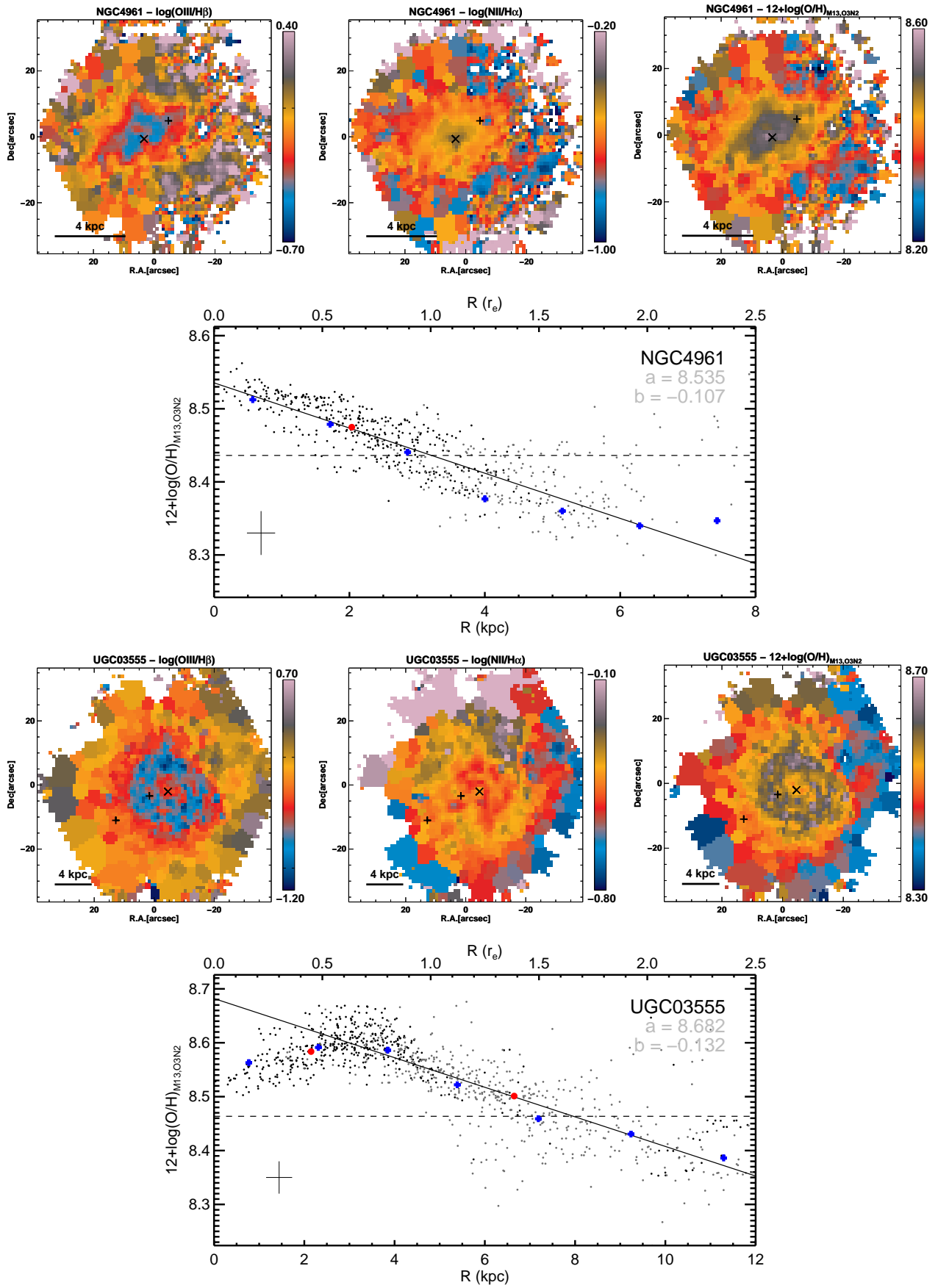


Fig. 1. NGC 4961 and UGC 03555 OIII/H β , NII/H α , and oxygen abundance maps (top) and gradient fits (bottom). Black dots are measurements in individual spaxels, grey dots are measurements in Voronoi spaxels, blue dots are measurements from azimuthal averaged spectra, and red dots are measurements from the spaxels where SNe exploded (2001ee-II in the top figure, and 2004ge-Ic/1999ed-II in the bottom figure). Mean representative X- and Y- errors are plotted in the lower-left corner for reference.

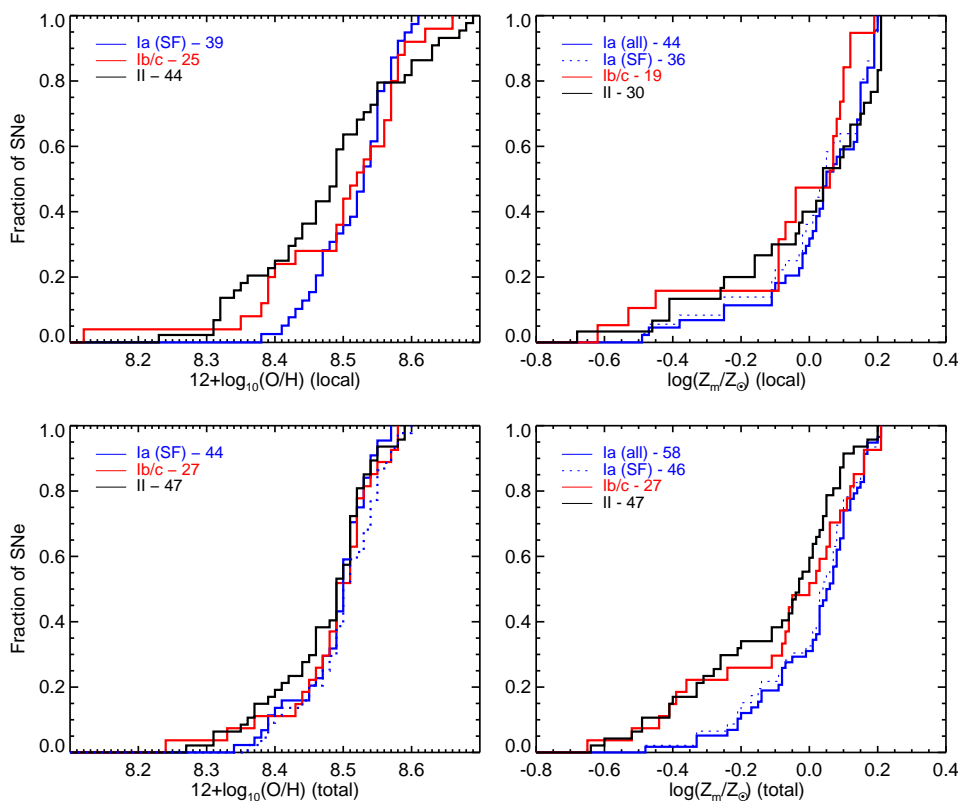


Fig. 2. SN environment measurements of the oxygen abundance (left) and the mass-weighted stellar metallicity (right) for galaxies hosting different SN types. In the top row we show the distributions of the local metallicity while in the bottom row total metallicity distributions are plotted. The ordinate indicates the fraction of the SN population with metallicities less than the abscissa value.

tions are small, it is worthy noting that SN Ia have the highest metallicity of the three SN types.

The lower row of Fig. 2 shows the cumulative distributions of the total galaxy metallicity. The gas-phase metallicity of the three SN types hosts is on average very similar for the three SN types (~ 8.48 dex) and the distributions are statistically indistinguishable. However, similarly to the metallicity at the SN locations the standard deviation of the distribution of SNe Ia hosts is smaller than the core-collapse SNe. The total stellar metallicity shows noticeably larger differences between the three SN types, with the difference between SN Ia and SN II being statistically significant. Again, even though the differences are small, SN Ia have the highest metallicity of the three SN types.

Figure 3 shows the cumulative distributions of the difference between the local and the global metallicity. The properties of the distributions are given in Table 5. All distributions are centered close to the zero, but there are small differences between the SN types. The local gas-phase metallicity of SN Ia is on average 0.03 dex higher than the total galaxy metallicity and this is the only difference that is statistically significant. The differences between the local and the global stellar metallicities is not significant for any SN type.

4.2. Other proxies of the local metallicity

In the past several indirect measurements have been used to estimate the metallicity at the SN location. The spatially resolved spectroscopy nature of our data allowed us to estimate the metallicity at the SN position and at the same time to compare it to the metallicity at the SN location estimated by other approximations. Therefore, we are in a position to test whether such methods are good proxies for the local SN metallicity.

In the previous Section we have shown that the metallicity measured from the total galaxy spectrum is a fair approximation of the local metallicity. In this Section we focus on several other

Table 4. Properties of the distributions of the gas-phase and stellar metallicities at the SN location and the total galaxy. Shown are the mean, the standard deviation σ , the standard deviation of the mean σ_m , the median and the number of SNe.

SN type	mean	σ	σ_m	median	N
$12+\log(\text{O}/\text{H})_{\text{local}}$					
Ia	8.522	0.056	0.009	8.537	39
Ib/c	8.500	0.114	0.023	8.520	25
II	8.484	0.112	0.017	8.494	44
$12+\log(\text{O}/\text{H})_{\text{total}}$					
Ia	8.492	0.054	0.008	8.505	44
Ib/c	8.489	0.076	0.015	8.500	27
II	8.477	0.074	0.011	8.500	47
$\log(Z_m/Z_\odot)_{\text{local}}$					
Ia	0.032	0.173	0.026	0.052	44
Ib/c	-0.049	0.232	0.053	0.067	19
II	-0.012	0.238	0.043	0.043	30
$\log(Z_m/Z_\odot)_{\text{total}}$					
Ia	0.021	0.149	0.020	0.060	58
Ib/c	-0.069	0.239	0.046	0.007	27
II	-0.105	0.223	0.033	-0.022	47

proxies. The results of these proxies are given in Table 5 for the three SN types and explained below.

4.2.1. Central metallicity

The Sloan Digital Sky Survey and other galaxy surveys use fiber spectrographs to provide thousands of spectra of the central regions of galaxies in the nearby Universe. Such surveys can be very useful for SN studies (see e.g., Prieto et al. 2008), but this approach has several drawbacks. Galaxies with AGN cannot be used because the strong line methods for gas-phase metallicity

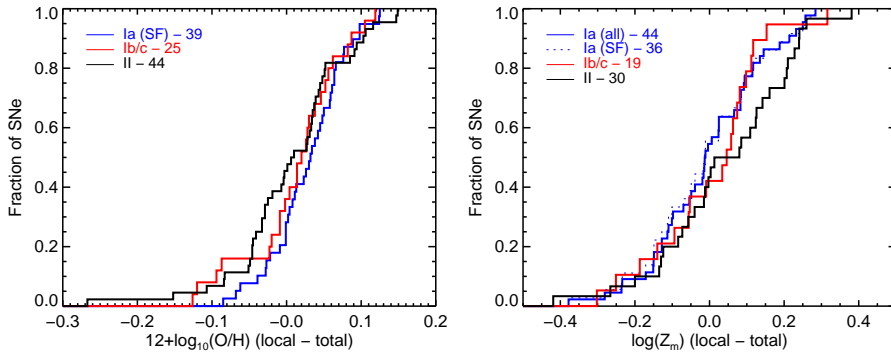


Fig. 3. Differences between the local and the total oxygen abundance (left) and mass-weighted stellar metallicity (right) for different SN types.

estimate are no longer valid. As we discuss in Appendix A, a large fraction of the galaxies in our sample have AGNs. More specifically, 59% of the star-forming SN Ia hosts (27 of the 46), 22% of SN Ib/c/IIb hosts (6 out of 27) and 32% of SN II hosts (15 out of the 47) have AGNs. As we have already shown in Paper I, there is a higher ratio of SN Ia host galaxies that have an AGN compared to the galaxies that hosted other SN types. This ratio would increase to 67% if the 11 elliptical galaxies, all of which host an AGN, are included.

Figure 4 shows the distribution of the differences between the local metallicity and the metallicity measured at the galaxy core only for those galaxies with both measurements available. For the gas-phase metallicity all distributions have negative mean values and thus the central metallicity is an overestimation of the metallicity at the SN position. The offsets are not large, -0.018 , -0.025 and -0.055 dex for SN Ia, Ib/c and II, respectively, and only the one for SN II is statistically significant. The smallest offset for SNe Ia could be explained by the metallicity decrease towards the center in some galaxies (see previous section). More than half of SN Ia hosts in our sample have such decrease, which would center the distribution toward zero. The fraction of galaxies with the central decrease among the CC SN hosts is lower and hence the offset is larger. The difference of the stellar metallicities are -0.088 , -0.083 and -0.030 dex for SN Ia, Ib/c and II, respectively, with only the first two being statistically significant. The corresponding standard deviations are $\sigma_{\text{Ia}}=0.19$, $\sigma_{\text{Ib/c}}=0.13$ and $\sigma_{\text{II}}=0.32$ dex. These results indicate the error if the central metallicity is used as a proxy for the local metallicity. However, because the standard deviation and the offset from zero are both larger than that for the total metallicity, its accuracy is lower.

Our findings agree with those of Modjaz et al. (2011) who found that local metallicities of SN Ib/c in their sample were generally lower than the central ones. However their central estimation came from host galaxy luminosity and not from gas emission line ratios. Our results also agree with Sanders et al. (2012), who claims that central and local metallicities are equal within 0.1 dex (in PP04 scale).

4.2.2. Central metallicity plus characteristic metallicity gradient

Another approach to estimate the local metallicity is to use the central metallicity plus the characteristic metallicity gradient (in normalized units). This can be very useful to utilize galaxy surveys performed with multi-fiber spectrographs like SDSS, which for low-redshift galaxies provide only the central metallicity. We here normalized the individual metallicity gradients to a common ruler, the disc effective radius r_e , the radius containing half of the total integrated flux coming from the disc component. The procedure followed to estimate r_e is described in Appendix

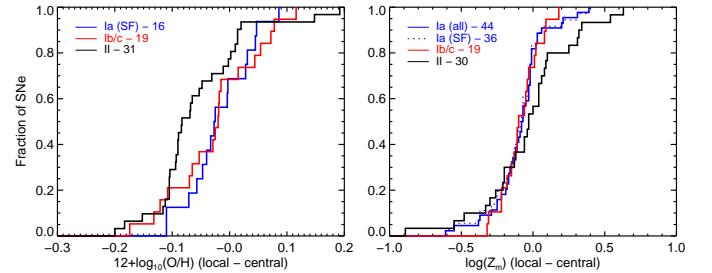


Fig. 4. Distributions of the differences between local and central metallicity.

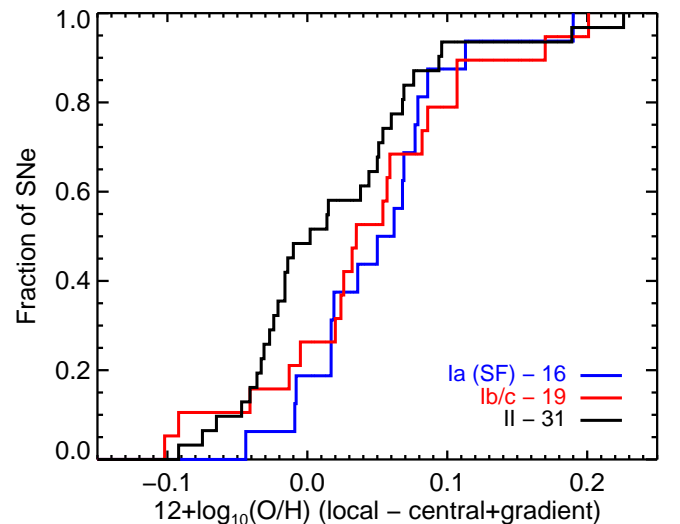


Fig. 5. Distribution of differences between local metallicity and the proxy using central metallicity plus characteristic gradient.

A. We have tested this approach and Fig. 5 shows CDFs of the differences. Of all proxies considered here, this one shows the largest mean differences and appears to be the least accurate one (Table 5). Only the difference for SN II is not statistically significant. The larger offset for SN Ia is likely due to the larger fraction of hosts with central metallicity decrease, which will bias this estimator.

4.2.3. Metallicity gradient and radial distance

Metallicity gradients measured with long-slit spectroscopy have been used to estimate the metallicity at the location of SN explosions. The gradients are usually measured by placing the slit along the galaxy major axis and then the metallicity at the radial distance of the SN is estimated. We estimated the gas-phase

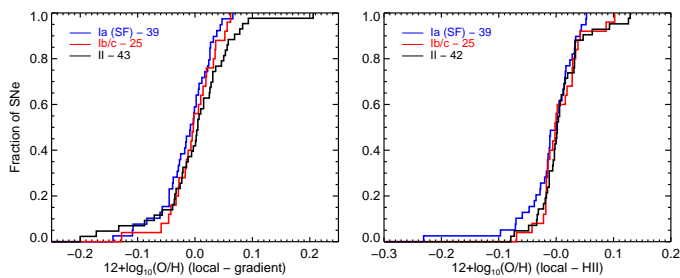


Fig. 6. Distribution of differences between local metallicity and the proxy using gradients (left) and the metallicity of the closest HII region (right). All measurements performed with O3N2 index.

metallicity at the SN location using the individual metallicity gradient for each galaxy obtained in Section 3.2 and the deprojected GCD of the SN. In the left panel of Figure 6 we show the distributions of the differences between the metallicity at the SN position and that estimated using the gradients. We see that all SN types have narrow distributions with standard deviations of $\sigma_{\text{Ia}}=0.085$, $\sigma_{\text{Ib/c}}=0.053$ and $\sigma_{\text{II}}=0.071$ dex, and no significant differences in the average values can be seen for different SN types. This is an indication that a (well-measured) metallicity gradient could be a good approximation to the value at SN position for SNe Ib/c and II. For SN Ia the total metallicity appears to be a better approximation.

4.2.4. Closest HII region

As in Paper I, HIIEXPLORER (Sánchez et al. 2012b) was used to extract HII regions from the extinction corrected H α emission maps. The caveats of this method are fully described in Paper I, but the main ones are that (i) we are actually selecting clumps of HII regions (1 to 6, Mast et al. 2014) instead of individual regions, especially in more distant galaxies; and (ii) this method tends to select regions with similar sizes, although this is not the case for real HII regions in galaxies.

For each SN, we determined the SN host HII region by selecting the clump that is closest to the SN location in terms of deprojected distance, and the spectra of the spaxels belonging to that HII region were co-added and analyzed. It is reasonable to consider that for CC SNe the progenitor might be formed in fainter HII regions not detected by this method. For SNe Ia it is difficult to associate the selected HII region as the place where the progenitor was formed as SNe Ia may have old progenitors, which might have migrated away from their birthplace.

In the right panel of Fig. 6 we show the distributions of the differences among the metallicity at the SN position and that of the closest HII region. All distributions are centered at zero within 0.01 dex and have small standard deviations ~ 0.04 dex³. The standard deviations are smaller than both the local metallicity estimates using gradients and the total metallicity, which means that the metallicity of the nearest HII region is a better approximation. This is expected because compared to the other proxies of the local metallicity, the nearest HII region is the most direct measurement.

³ The width of the distribution for SNe Ia larger, but this is because of a single deviating point. Once this point is removed, the distribution becomes the narrowest of all with standard deviation 0.03 dex.

Table 5. Properties of the distributions of the differences between the metallicity estimated from local measurements and the metallicity estimated using different proxies. Shown are the mean, the standard deviation σ , the standard deviation of the mean σ_m , the median and the number of SNe.

SN type	mean	σ	σ_m	median	N
$12+\log(\text{O}/\text{H})_{\text{local-total}}$					
Ia ^a	0.029	0.050	0.008	0.032	39
Ib/c	0.012	0.064	0.013	0.020	25
II	0.006	0.078	0.012	0.008	44
$12+\log(\text{O}/\text{H})_{\text{local-HII}}$					
Ia	-0.004	0.035	0.006	0.001	39
Ib/c	0.007	0.037	0.007	-0.001	25
II	0.008	0.042	0.006	0.002	42
$12+\log(\text{O}/\text{H})_{\text{local-gradient}}$					
Ia	-0.014	0.045	0.007	-0.007	39
Ib/c	-0.003	0.041	0.008	-0.002	25
II	0.001	0.069	0.011	0.005	43
$12+\log(\text{O}/\text{H})_{\text{local-central}}$					
Ia	-0.018	0.056	0.014	-0.026	16
Ib/c	-0.024	0.077	0.018	-0.019	19
II ^a	-0.056	0.082	0.015	-0.082	31
$12+\log(\text{O}/\text{H})_{\text{local-central+gradient}}$					
Ia ^a	0.052	0.056	0.014	0.057	16
Ib/c ^a	0.043	0.077	0.018	0.036	19
II	0.020	0.071	0.013	0.003	31
$\log(Z_m)_{\text{local-total}}$					
Ia	-0.004	0.150	0.023	-0.011	44
Ib/c	0.004	0.150	0.034	0.047	19
II	0.042	0.178	0.032	0.047	30
$\log(Z_m)_{\text{local-central}}$					
Ia ^a	-0.086	0.185	0.028	-0.070	44
Ib/c ^a	-0.083	0.131	0.030	-0.099	19
II	-0.029	0.311	0.057	-0.024	30

Notes. ^(a) statistically significant difference.

4.3. Aperture effects

At low redshift fiber spectrographs usually measure only the light from the central region of galaxies. As the redshift increases, the fraction of the galaxy light integrated by the fibers also increases. Comparing measurements obtained from different integration fractions of the galaxy introduces a bias in the results, and aperture effects must be accounted for. IFS makes it possible to extract spectra integrating the datacubes in different apertures to study how the galactic parameters change with the aperture. In this way we are able to simulate observations obtained with different fixed-size fibers or, what would be equivalent, observations with a fixed-size fiber of galaxies at different redshifts. This has been studied in detail in Iglesias-Páramo et al. (2013) with H α emission, in Iglesias-Páramo et al. (sub. to A&A) for oxygen abundances using the whole CALIFA galaxy sample, and in Gomes et al. (2015) with CALIFA early-type galaxies.

We calculated the spectra within 12 circular apertures centered at the galaxy cores and increasing the radii from 3 to 36'' in steps of 3''. The same procedure used for the individual spaxels was applied to measure the metallicities from each of the increasing aperture spectra. The left panel of Figure 7 shows the average values of the oxygen abundance for each SN type hosts as a function of an increasing aperture. The measurements lying in the AGN region of the BPT diagram are not considered

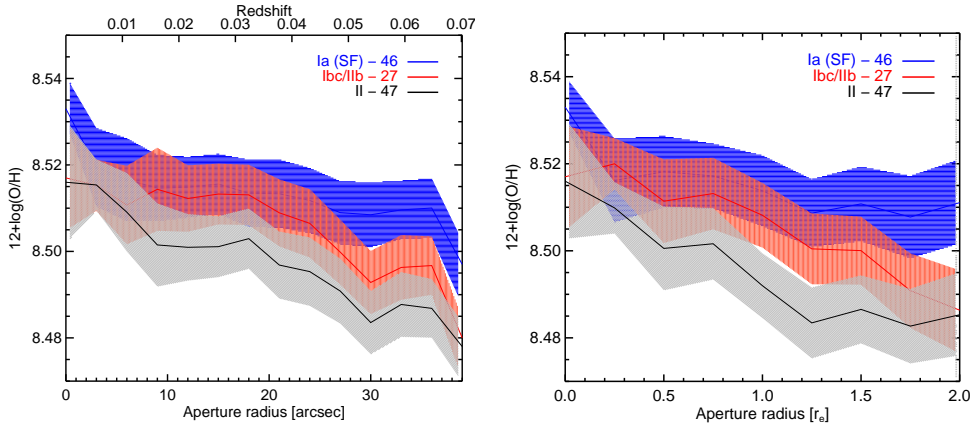


Fig. 7. Left: Mean values for oxygen abundance from the central spaxel (value at 0 arcsec) to the total spectra (value at 39 arcsec), increasing the aperture in steps of 3 arcsec. Error bands are errors of the mean values. The upper x-axis shows where the aperture with 3" diameter is projected for different redshifts. Right: Same measurements but normalizing the unit of the aperture to the effective radius of the galaxies.

in the construction of the averages of this measurement. On the right panel we show the same measurements but changing the radial scale to the disc effective radius of each galaxy. The differences between the central and the total values shown in the previous subsection arise here with the intermediate behaviors. We see that the average gas abundances decrease with increasing the aperture, and the hosts of the three SN types remain ordered as it is shown in the total distributions (See Fig. 2). The SN Ia band is above the two CC SN bands, and SN II show lower values than SN Ibc host galaxies. This behavior is easily explained (and expected) by the presence of metallicity gradients. As the aperture increases, new regions that are farther from the center are included in the integrated spectra. If these new regions are metal-poorer than their inner counterparts, the average of the aperture would be reduced, but not at the level of the metallicity of the new regions. Also remarkable is that in the two figures, SN Ia galaxies band is shallower compared to the CC SN host bands. Although passive galaxies are not included in the SN Ia group we show in Appendix B that the metallicity gradients of SN Ia hosts were also shallower. The maximum difference for any SN host is around 0.04 dex, and this would be an estimation of the systematic error when using fiber spectra measurements of galaxies spanning a wide range of redshifts.

A similar approach was used by González Delgado et al. (2015) who instead of studying how the stellar metallicity varies at increasing circular apertures, studied the deprojected radial profiles and gradients, splitting 300 galaxies from the CALIFA sample by morphology and mass. Their results are in agreement with our findings. Elliptical and S0 galaxies have higher stellar metallicities and flatter gradients than the late-type galaxies. This corresponds to our SN Ia group since these types of galaxies only host thermonuclear supernovae.

5. Discussion

5.1. Total metallicity

We have seen that the gas-phase and the mass-weighted stellar metallicities derived from the integrated galaxy spectra show different behavior for the three SN types (Fig. 2). The average gas-phase metallicity for the three SN types is nearly equal with differences less than 0.01 dex. The distributions are also similar. However, both CC SN types, Ibc and II, show more extended tail toward low metallicity, which is more prominent for SNe II. The average mass-weighted stellar metallicity on the other hand shows differences of ~ 0.05 dex between the three SN types. This behavior results from the distribution of the masses of the galaxies in our sample on one hand and the shape of the mass-

metallicity ($M - Z$) relation for the gas-phase and the stellar metallicities on the other.

Figure 8a shows the cumulative distribution of the current stellar mass of the galaxies in our sample by SN type. As already noted in Paper I, the mass distribution shows 0.3 – 0.4 dex difference between the mean masses of SN Ia hosts and those of the two CC SNe types. It can also be seen that about 90% of the SN Ia hosts and 60–70% of the CC SN hosts have masses above $\log(M/M_{\odot}) \simeq 10.3$ dex.

The $M - Z$ relations for the gas-phase metallicity and mass-weighted stellar metallicities are shown in Fig. 8b and c. The dotted lines in Figs. 8b and c show the $M - Z$ relation for the gas-phase metallicity derived Sánchez et al. (2013) from CALIFA observations. This relation describes the $M - Z$ relation for the gas-phase metallicity of the galaxies in our sample very well⁴, but from Fig. 8c it is evident that the mass-weighted stellar metallicity $M - Z$ relation is much steeper, in accordance with the findings of González Delgado et al. (2014). The solid line in Fig. 8c shows the Panter et al. (2008) $M - Z$ relation, which clearly describes the stellar metallicity $M - Z$ relation better. One can also see that both, the gas-phase and the stellar metallicity $M - Z$ relations present lower scatter above $\log(M/M_{\odot}) \simeq 10.4$ dex.

The fact that the gas-phase $M - Z$ relation is tighter and flatter than the stellar metallicity and that $\geq 80\%$ galaxies in our sample have masses higher than $\log(M/M_{\odot}) \simeq 10.3$ dex is the main reason why there are only very small differences between the average gas-phase metallicities for the three SN types. On the other hand, the stellar metallicity $M - Z$ relation is steeper and this is the most likely reason for the observed larger differences in the average stellar metallicities.

The small differences between the total gas-phase metallicity of different SN type host galaxies that we find is somehow at odds with the previously reported larger differences (see, e.g., Prieto et al. 2008; Shao et al. 2014). This is however most likely due to the bias toward higher masses in our sample. To clarify the possible impact in our results of this bias we have extended the study using data from the literature. Figure 9 shows the CDFs of the host masses of our SN Ia and CC SN samples, including the galaxies with SNe outside of FoV, compared to the targeted and the untargeted samples from Neill et al. (2009), Kelly et al. (2010), Kelly & Kirshner (2012),

⁴ Strictly speaking this relation is derived for oxygen abundance at the effective radius r_e . However, as Sánchez et al. (2013) also noted, we found that the difference between the metallicity at r_e is very close to the total metallicity estimated from the integrated spectra. The average difference we found was ~ 0.02 dex with 1σ scatter around 0.03 dex.

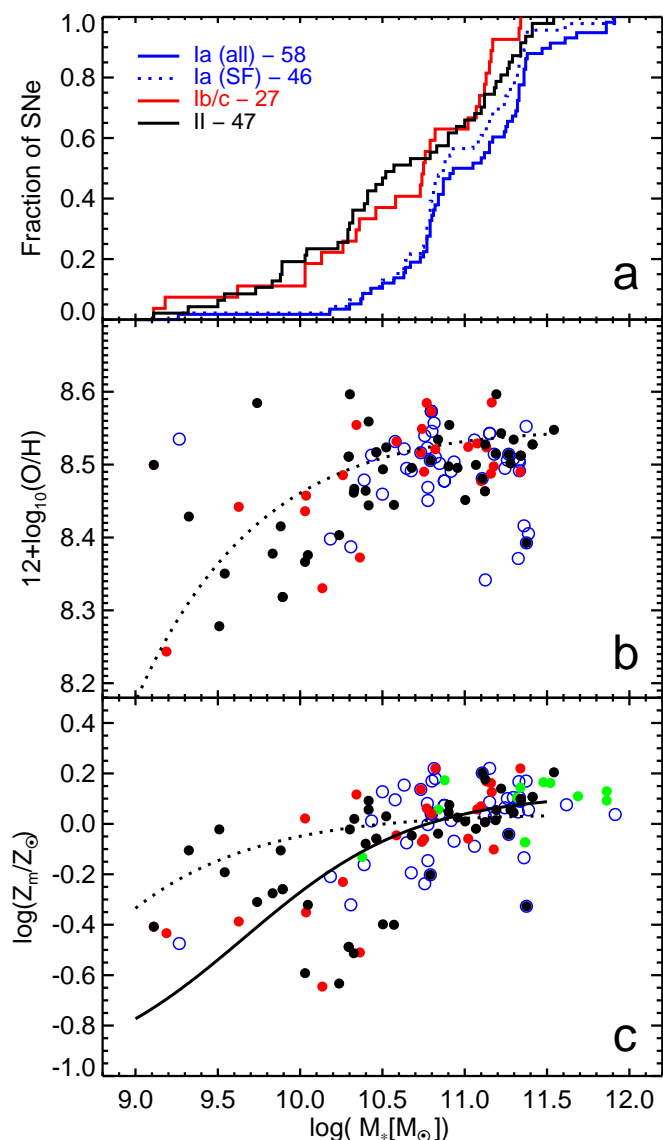


Fig. 8. *a* - cumulative distributions of the galaxies stellar mass; *b* - mass *vs.* gas-phase metallicity. The dotted line is the $M-Z$ relation from Sánchez et al. (2013) converted from PP04 to M13 version of the O3N2 calibrator. *c* - mass *vs.* mass-weighted stellar metallicity. The dotted line is the $M-Z$ relation from Sánchez et al. (2013) and the solid line is the Panter et al. (2008) relation. The green dots show the elliptical SN Ia hosts.

Childress et al. (2013), Stoll et al. (2013) and Pan et al. (2014). Table 6 gives details of the properties of the corresponding distributions. In these works different IFMs have been employed and we applied small corrections ($\sim 0.04-0.20$ dex; Bell et al. 2003; Sullivan et al. 2010) to convert the masses to Salpeter (1955) IMF. However, additional systematic differences are almost certainly present because of the use of different recipes to construct the fitting galaxy templates, different observational data used (photometry and spectroscopy) and different fitting approaches. Quantifying these differences is beyond the scope of this paper but they should be kept in mind when combining galaxy masses from different sources.

The data from the literature clearly shows that the targeted surveys suffer from a bias toward massive galaxies, which is ~ 0.77 dex for SNe Ia and ~ 0.9 dex for the CC SNe. It is also evident that our sample, which consists of SNe discovered

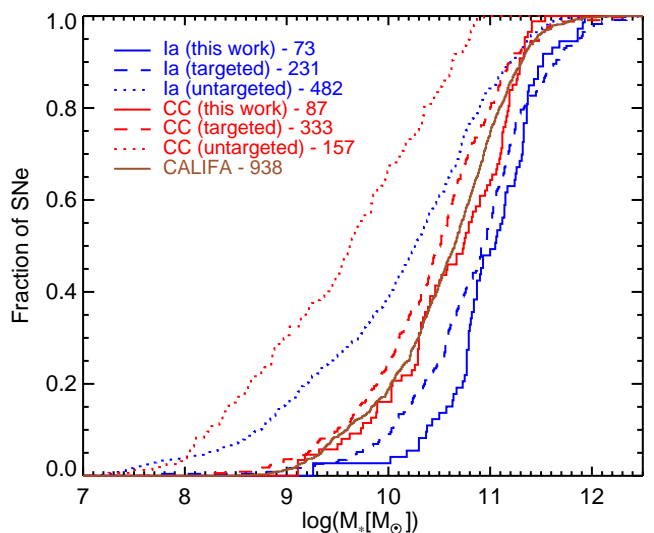


Fig. 9. CDFs of the host galaxy masses of various SN Ia and CC SNe samples (see the text for details).

Table 6. Statistics of the distributions of galaxy masses in different SN samples in units of $\log(M/M_\odot)$. For each SN sub-type are shown the mean, the standard deviation σ and the median.

	SN Ia			CC SN		
	mean	σ	median	mean	RMS	median
This work	11.00	0.50	11.06	10.61	0.62	10.74
Targeted:	10.85	0.66	10.94	10.42	0.68	10.51
Untargeted	10.08	0.98	10.27	9.52	0.88	9.62

by targeted searches, is biased even more toward higher masses; with respect to the targeted sample from the literature this bias for both SN Ia and CC SN is ~ 0.15 dex. The mean masses of both SN Ia and CC SNe hosts found in targeted searches are in the range $\log(M/M_\odot) \approx 10.4 - 10.7$ and with only a small fraction of SNe (~ 10 and 20% for SN Ia and CC SN, respectively) present in galaxies with masses below $\log(M/M_\odot) \approx 10.3$ dex. Because of the lower scatter in the $M-Z$ relation above $\log(M/M_\odot) \approx 10.3$ dex, the metallicity differences between the SN types should be small in samples from targeted searches. The untargeted searches on the other hand include galaxies with lower masses in the range where the $M-Z$ relation is steeper and the metallicity differences, if significant, will be more pronounced.

5.2. Local metallicity

We have estimated both the gas-phase and stellar metallicities at the SN locations. As discussed in Stanishev et al. (2012) the stellar metallicities are estimated with much greater uncertainty due to various factors including astrophysical and numerical degeneracies, noise in the observed spectra, uncertainties in the recipes to construct the SSPs, etc. Even without these uncertainties, the S/N in the continuum of the binned spectra at the SN location may not be enough to estimate the metallicity accurately enough. For this reason we focus our discussion of the local metallicity to the gas-phase oxygen abundance.

We found only small differences between the average metallicity at the SN locations for the three SN types, 8.522, 8.500 and 8.484 dex for SN Ia, Ibc and II, respectively. These differences are considerably smaller than the 1σ scatter, which is 0.056 dex

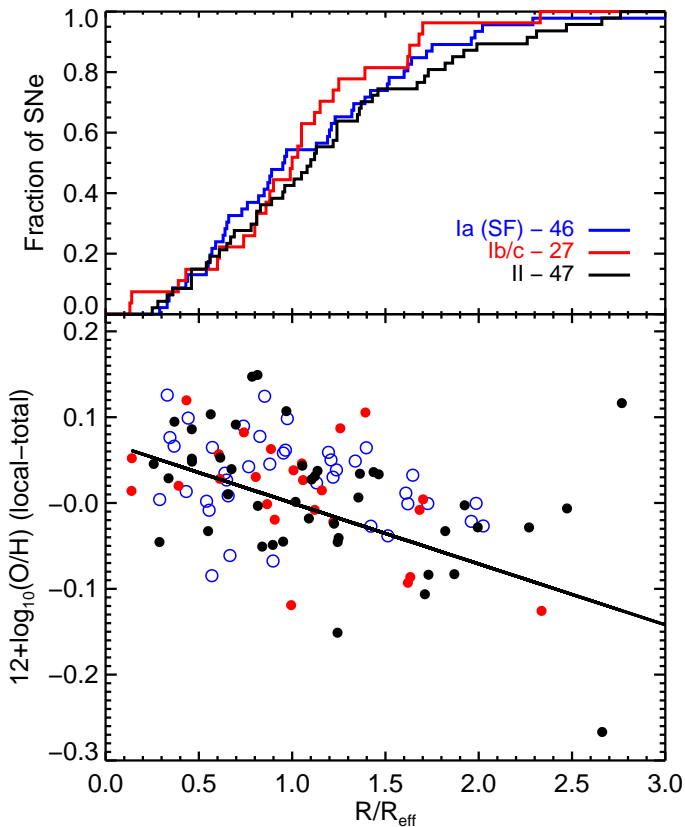


Fig. 10. Upper panel: CDFs of the normalized radial distribution of the different SN types. Lower panel: difference between the local and the total metallicity as function of the normalized GCD. The line is a guide-to-the-eye and has a slope of -0.074 – the average metallicity gradient of the galaxies in our sample.

for SN Ia and 0.112 dex for the CC SNe. However, one question that should be addressed is whether what we measure is the local metallicity at the SN position. As the distance to the galaxies increases it becomes more difficult to measure local quantities because of the decrease of the spatial resolution when observing with fixed-size slits or fibers. Recently, Niino et al. (2015) studied how the variation of the metallicity within a galaxy and the spatial resolution affect the local metallicity estimation. They found that when the resolution is lower than 500 pc, the local metallicity could be accurately estimated. Resolution up to 1 kpc also provide reasonable estimates, although some systematic effects are present. When the resolution is larger than 1 kpc the constrain of the local metallicity becomes more uncertain. For the redshift range of our targets from 0.005 to 0.03 the resolution of the CALIFA maps (PSF ~ 2.57 arcsec) corresponds to a spatial resolution between ~ 250 pc and 1.5 kpc. However, only a small fraction of our targets are at the higher end of the redshift distribution and on average the resolution effects will be small in our sample.

The fact that the differences between the local metallicities of the different SN types in our sample are small are not surprising because the total metallicities estimated from the integrated spectra are on average also the same and the galaxies seem to have a characteristic metallicity gradient in normalized radii units. Given this, large differences between the local metallicities can be observed if (i) the different SN types have significantly different radial distributions or (ii) the galaxies contain regions with metallicity, which are significantly different from

the galaxy average. In the latter case, if certain SN type prefers to explode in low or high-metallicity environment, then the local metallicity of this SN type will tend to differ from the galaxy average. However, a careful inspection of the 2D metallicity maps shows that regions with significantly different metallicity from the average are rare or absent, because the dynamical range of abundances across the entire galaxy is small.

The analysis of the SN radial distances shows that SNe Ib/c tend to explode slightly closer (by less than 1 kpc) to the galaxy center than SNe II, and SNe Ia on average 1 kpc further away than SNe II. However, once the distance are normalized to the effective radius R_{eff} all distributions have similar averages of 1.1 , 1.0 and $1.2R_{\text{eff}}$ for SN Ia, Ib/c and II, respectively. This is in agreement with previous statistical studies of SNe radial distributions (Bartunov et al. 1992; van den Bergh 1997; Tsvetkov et al. 2004; Petrosian et al. 2005; Prieto et al. 2008; Hakobyan et al. 2009; Anderson & James 2009). The upper panel of Figure 10 shows the distribution of the de-projected distances measured in disk effective radius units. In the bottom panel of Fig. 10 the difference between the local and the total metallicities as function the normalized deprojected distances is shown. The difference decreases with the radial distance for all SN types at a rate consistent with the average metallicity gradient (the line with slope of -0.074 guides the eye). From the figure one can see that SNe Ia tend to be slightly above the line and hence they show larger average difference than the CC SNe. However, the difference is rather small and could be caused by other effects, for example by slightly biased estimation of the total galaxy metallicity.

From Fig. 10b one can see that the metallicity at the SN location follows the galaxy mean metallicity and that it also changes with the radial distance following the metallicity gradients. However, the scatter of the difference between the local and the total metallicities, and the scatter around the line is considerable, ~ 0.05 dex. One interesting question is whether part of this scatter arises because some SNe preferably explode in regions with higher metallicities. Because many galaxies have negative metallicity gradients, if that was the case, SNe may tend to explode closer to the galaxy center. However, the density of the stars in the galaxies and the SFR also increase toward the center and statistically one can expect to find more SNe toward the central regions. Thus, the two effects will be difficult to disentangle.

Galaxies typically have central symmetry. One way to test the hypothesis that some SNe prefer to explode in high-metallicity regions is to look at the difference between the metallicity at the SN position and the mean value of the galaxy metallicity at the radial distance of the SN. To estimate the latter, the mean metallicity and the standard deviation of the individual spaxels within 1 kpc of the deprojected GCD of the SNe were computed. In Fig. 11 are shown the distributions of the differences divided by the standard deviation. For all SN types the mean differences are essentially zero and the distributions are narrow with standard deviations of about one. SN II show slightly wider distribution than the other SN types. This indicates that on average the metallicity at the SN location does not differ significantly from the galaxy average at the SN radial distance. There is only a small hint for an extended tail toward lower metallicities for SN II.

5.2.1. Proxies of local metallicity

We have compared the directly estimated local metallicities obtained with IFS with several other approaches that have been

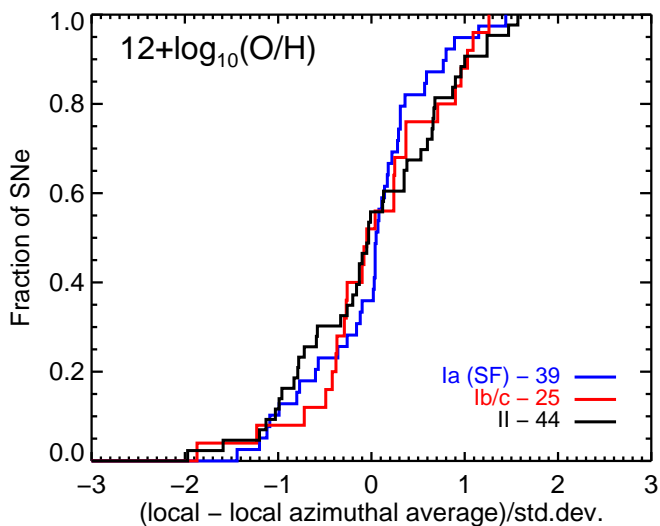


Fig. 11. Difference between the oxygen abundance at SN position compared to the azimuthal average at that distance, normalized to the standard deviation of the abundance at that distance.

used as proxies of local metallicity estimations. We conclude that the central metallicity, with and without a correction assuming characteristic metallicity gradient is the least accurate one. It has both larger bias and scatter. Not surprisingly, the metallicity of the closest H II region and the one estimated from each galaxy’s individual metallicity gradient are the best proxies of the local metallicity. However, these two methods are applicable to nearby galaxies only and are likely of little practical use, e.g. for high-redshift SN Ia studies. On the other hand, the total galaxy metallicity appears to be the best compromise. It has relatively small bias and scatter. In addition, it is a quantity that can be easily measured for galaxies at high redshifts.

The likely reason for the similarity between the local and total metallicities is that in low-redshift galaxies the metallicity gradients are fairly shallow. However, one should have in mind that this may not be the case for high-redshifts galaxies and hence the total metallicity may not be as good proxy as at low redshift.

5.2.2. Differences among SN subtypes

Our primary goal is to explore the connection between the SN environmental metallicity and the nature of the progenitors for each SN type. At present, the CALIFA sample used in our analysis is not sufficiently large to allow splitting of the two main CC SN groups into further sub-classes with enough events. In addition, the vast majority of our sample comes from targeted searches and is biased toward high-mass, metal-rich galaxies. As a result the local metallicity we measure is very similar for all SNe. For the above reasons we combined our values with measurements of the metallicity at SN locations from the literature. This enlarged sample contains SNe discovered by both targeted and untargeted surveys. We considered only measurements performed at the SN location or close vicinity and whenever repeated we rely on our measurements. The compiled sample includes all the measurements from: Thöne et al. (2009); Young et al. (2010); Modjaz et al. (2011); Anderson et al. (2011); Prieto et al. (2012); Kuncarayakti et al. (2013a,b); Tomasella et al. (2013); and only those reported as local from: Anderson et al. (2010); Leloudas et al. (2011); Sanders et al. (2012); Habbergham et al. (2012), and Moreno-Raya et al.

(2016). In addition, we included metallicities of 11 SNe in galaxies observed with the new MUSE IFS (Galbany et al. 2016a). Following Sanders et al. (2012), we did not include Kelly & Kirshner (2012) since those are measurements from the center of the galaxies.

Since many different calibrators are used, we considered only those using PP04 O3N2 calibrator and converted them to the M13 scale. However, this sample can be further enlarged if we also consider those measurements computed with the PP04 N2 calibrator, and converted to O3N2 scale using the relation produced by Kewley & Ellison (2008). In this enlarged sample we used data from: Stoll et al. (2013); Sahu et al. (2009); Levesque et al. (2010); Milisavljevic et al. (2013); Inserra et al. (2013); Van Dyk et al. (2012); Taddia et al. (2013) and Taddia et al. (2015). We also added the metallicities of the SN Ia hosts from the untargeted searches reported in Pan et al. (2014) and Childress et al. (2013). These metallicities were measured with long-slit spectroscopy and the manner the spectra were extracted from the 2D images means that they are close to the galaxies total metallicity. However, in our sample the local and the total metallicities of SN Ia hosts differ on average by 0.029 dex and we can use Pan et al. (2014) and Childress et al. (2013) measurements as proxy of the local metallicity.

We considered the following main SN classes: Ia, Ib, Ic, broad-line Ic (IcBL), II, IIn and IIb. Recently, the presence of two different populations of SN II (IIP and IIL) has been put in question. While some works (Arcavi et al. 2012; Faran et al. 2014) present evidence for two separated populations, this has been questioned by a number of works (Anderson et al. 2014; Sanders et al. 2015; Galbany et al. 2016b) which argued that this is really a continuous between slow- and fast-decliners, and the traditional division was due to the low number of SNe IIL. Following the latter works, we put SNe IIP and IIL in one group II. We also consider separate classes of SNe Ib and IIb, but because these are probably closely related (by a continuous sequence of the amount of Hydrogen in their outer layers) we also computed the mean metallicity of SNe Ib and IIb together. Many SNe Ib/c have uncertain classification. These were grouped with SNe Ib/c with certain classification to compute the mean metallicity of the combined SN Ib/c class. The mean metallicity of the whole CC SN class was also computed excluding the broad-line SNe Ic.

Further, the sample was divided into two groups – SNe discovered by targeted or untargeted searches. The resulting distributions of the oxygen abundance are shown in Figure 12. The properties of the distributions for all SN types are summarized in Table 7 and the p-values of the KS tests are listed in Table 8. The CALIFA sample presented in this work comprises mostly of SNe discovered in targeted searches and thus it only makes significant contribution to the targeted SN sample.

Metallicity at the SN Ia locations

The locations of SNe Ia are most likely not related at all to the birth place of the progenitor star due to their long delay times (100 Myrs to Gyrs), thus progenitors could have travelled across the galaxy a considerable distance before explosion as supernovae. Any association between SN environment observed properties and the SN progenitor population is much more problematic, however, the study of the properties of SN Ia environments can give insights on the characteristics of the explosion that might be useful, for example, for cosmological analyses.

SNe Ia have the highest mean metallicity at the SN location in the targeted sample (8.52 dex) and similar to SN II and

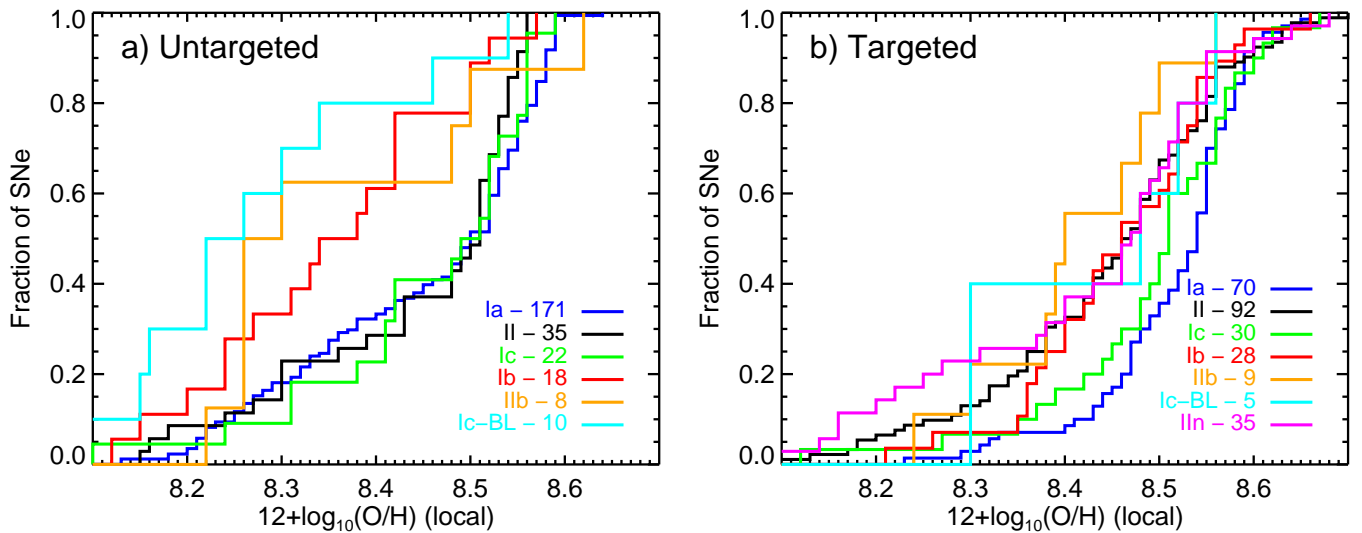


Fig. 12. Compilation of the oxygen abundances at the SN location measured in this work combined with previously published from the literature. We combined published measurements using the O3N2 calibrator with measurements using the N2 converted to O3N2 with [Kewley & Ellison \(2008\)](#) relation. *a*) – for SNe discovered in untargeted searches; *b*) – in targeted searches. The CALIFA sample presented in this work contributes essentially to the targeted sample.

Table 7. Statistics of the local metallicity distributions of SNe discovered in untargeted and targeted searches. For each SN sub-type are shown the mean, the standard deviation σ , the standard deviation of the mean σ_m , the median, and the number of SNe.

type	untargeted					targeted				
	mean	σ	σ_m	median	N_{SN}	mean	σ	σ_m	median	N_{SN}
Ia ^a	8.455	0.129	0.010	8.503	171	8.520	0.083	0.010	8.543	70
Ic	8.458	0.124	0.026	8.515	22	8.495	0.112	0.020	8.511	30
II	8.447	0.126	0.021	8.511	35	8.450	0.127	0.013	8.475	92
IIb	8.367	0.149	0.053	8.302	8	8.415	0.101	0.034	8.404	9
Ib	8.355	0.130	0.031	8.388	18	8.461	0.102	0.019	8.468	28
Ic-bl	8.274	0.151	0.048	8.261	10	8.436	0.123	0.055	8.481	5
Ib/IIb	8.359	0.133	0.026	8.344	26	8.450	0.100	0.016	8.448	39
Ibc	8.418	0.133	0.020	8.428	44	8.485	0.107	0.014	8.511	62
IIIn	—	—	—	—	—	8.427	0.150	0.025	8.475	35
CC	8.421	0.137	0.015	8.488	88	8.455	0.126	0.009	8.481	196

Notes. ^(a) The metallicities of the untargeted SN Ia sample come from [Pan et al. \(2014\)](#) and [Childress et al. \(2013\)](#). These measurements correspond to the total galaxy metallicity and have been corrected by +0.028 dex to account for the bias. See text for details.

Ic in the untargeted (8.46 dex). However, most the untargeted SN Ia come from measurements similar to the total metallicity, corrected for the small bias. [Pan et al. \(2014\)](#) sample has higher mean metallicity 8.53 dex (corrected for the bias), but the mean of the whole sample is pushed toward low metallicity by the sample of [Childress et al. \(2013\)](#). This comes from the fact that the latter sample also has significantly lower mean mass.

If we take the mean masses of SN Ia hosts from Table 6 in the targeted and untargeted samples and compute the corresponding metallicities with the $M - Z$ relation of [Sánchez et al. \(2013\)](#) we get 8.53 and 8.47 dex for SNe Ia in the combined targeted and untargeted samples, respectively. the same analysis for CC SNe hosts gives metallicities of 8.50 and 8.36 dex. However, if we apply the $M - Z$ relation for our sample only, we obtain metallicities of 8.53 and 8.50 dex, for SN Ia and CC SN hosts respectively. These numbers are very close to the actual estimated mean metallicities, except for CC SNe in the untargeted sample, which deviate by 0.06 dex. This suggest that the difference in

the mean metallicity on the different samples is to large extent due to the $M - Z$ relation.

Metallicity at the CC SN locations

From Table 7 we see that all SN types, except for SN II, show bias toward higher metallicity in the targeted samples. The bias is different for the different types, and SN Ib and Ic-BL are particularly affected (>0.1 dex). In the targeted sample SN Ic locations show higher Z than both SN Ib and SN II locations, and the latter also show Z similar to SN IIIn and SN Ic-bl. SN IIb is the CC SN subtype with the lowest average Z . The picture changes for the untargeted sample: while SN II and SN Ic now show similar Z , SN Ib have significantly lower Z , but similar to SN IIb. SN Ic-BL are, as expected, in the lowest Z end. So, from the untargeted SNe we have the following sequence:

$$Z_{\text{Ic}} \gtrsim Z_{\text{II}} > Z_{\text{Ib}} \gtrsim Z_{\text{IIb}} > Z_{\text{Ic-BL}}. \quad (1)$$

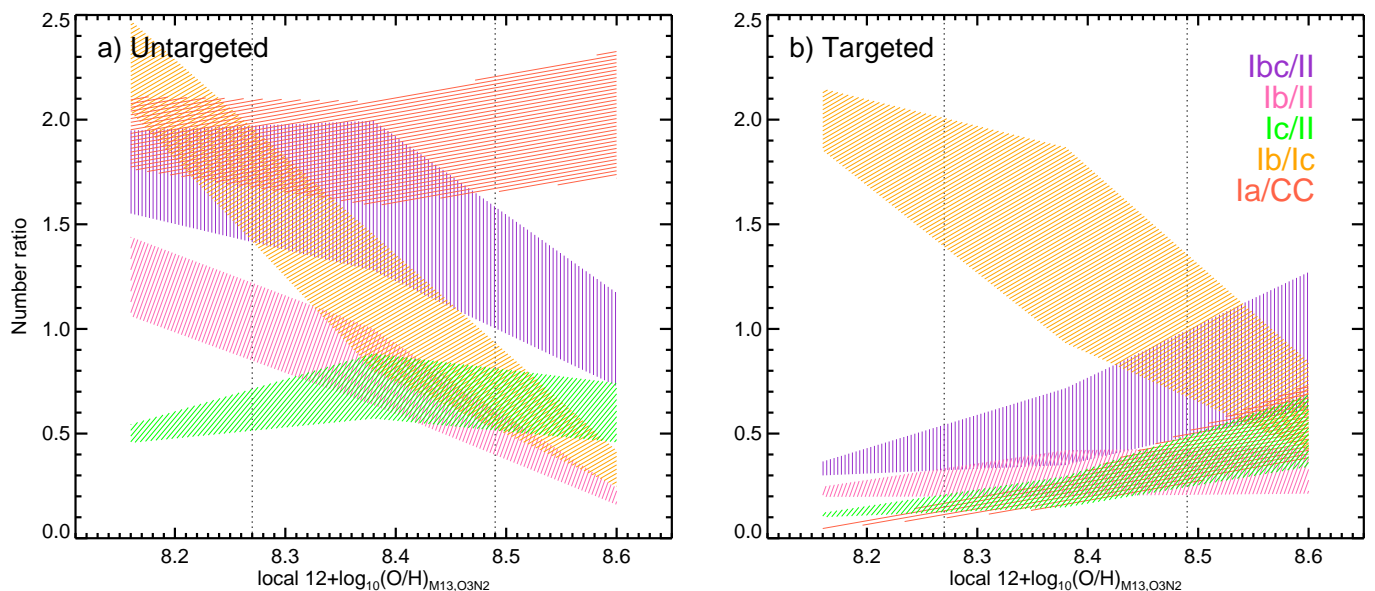


Fig. 13. Ratio of SN subtypes as a function of local metallicity from the compilation of the oxygen abundances at the SN location measured in this work combined with previously published from the literature. *a)* – for SNe discovered in untargeted searches; *b)* – in targeted searches.

The differences in the mean local metallicities are generally small and in most cases probably insignificant. KS test indicated that SNe Ic and II probably came from the same metallicity distribution, which is different from that of SN Ib, Iib and Ic-BL.

Furthermore, we studied how the number ratios between two subtypes evolve with the environmental metallicity increase. In Figure 13 we present the results of several of these ratios measured in three metallicity bins centered at 8.16 (below solar), 8.38 (around solar), and 8.60 dex (above solar). The analysis is split for untargeted and targeted samples.

In general, the behavior of the ratios is different in the targeted and untargeted samples, with the exception of the Ib/Ic ratio that decreases with metallicity in both samples. While in the untargeted sample the Ic/II ratio is practically flat with a soft increase to high metallicity, in the targeted sample it clearly increases. Indeed, as we have seen in Figure 12, there is no significant difference in the untargeted SN Ic and II distributions, while the difference is higher in the targeted sample. We also found an increasing rate of targeted SNe Ibc over SNe II as previously found by Arcavi et al. (2010); Prantzos & Boissier (2003); Prieto et al. (2008) and Kelly & Kirshner (2012), however, when we consider only the untargeted sample this ratio goes in the opposite direction. By studying the relative rates between the different components we see that this evolution is driven by the decreasing number of SNe Ib at higher metallicities: while the ratio between Ib and II is practically flat for the three regimes in the targeted sample, it shows a steep decrease in the untargeted sample. Therefore, any difference in the evolution of SN Ibc when compared to SN II is caused by the lower metallicity of SN Ib compared to Ic, in any targeted or untargeted samples.

Also, the proportion of SNe Ia over all CC SN types increases with the environmental metallicity, as we already found in this and previous sections: although SNe Ia also occur in metal-poor environments, their ratio is significantly higher in the metal-rich regime compared to all CC SN types. The increase is more pronounced in the targeted sample, and flatter in the untargeted sample.

The influence of metallicity in determining CC SN subtype

Differences in the evolution of SN type ratios with metallicity may be used to connect SN types to possible progenitor scenarios. Both the wind strength and the binary mass transfer rate are the plausible scenarios through which SNe Ibc lose their external layers. Another possibility may be that external H and He layers of the progenitor suffer severe depletion by enhanced mixing preventing their detection (Frey et al. 2013), although this would be difficult to assess from environmental studies.

According to the models based on the evolution of single massive stars (e.g. Heger et al. 2003; Georgy et al. 2009) both high metallicities and high initial masses are required to produce SNe Ibc in single stars, while in binary systems the mass loss is dominated by mass transfer and the models predict less significant trend with metallicity. If the primary SN Ibc progenitor channel is a single WR star then the rate of SN Ibc relative to SNe II would be enhanced at higher metallicities. Although this is what we found when considering SN discovered on targeted searches, the picture gets more complicated in untargeted SN: while the ratio between SN Ibc and II decreases with increasing metallicity, it is driven by the lower local metallicities at SN Ib positions. The strongest result we found is that SNe Ic, which are stripped of their H and He external layers, happen on average in significantly higher metallicity environments than SN Ib, which only lacks of the H envelope. These SN progenitors are in general short-lived, so there is a higher probability of SN local environmental metallicity to be related to the metallicity of the progenitor. The ratios presented in Figure 13 would imply that at least part of the progenitors of SNe Ic are single stars in strong metallicity driven wind environments, while the remaining SN Ic and a significant part of SN Ib and also SN Iib arise from binary progenitors (Claeys et al. 2011; Sana et al. 2012). This picture is supported by the results from Kuncarayakti et al. (2013a) that inferred lower masses from the stellar population ages for SN Ib compared to SN Ic. In addition, the flat ratio of untargeted SN Ic over SN II would imply that metallicity is not playing a

Table 8. P-values of the KS test for local distributions presented in Figure 12.

	Targeted	Untargeted
Ia-II	0.0002	0.0975
Ia-Ic	0.1434	0.6226
Ia-Ib	0.0108	0.0037
Ia-Ibc	0.0633	0.0420
Ia-IIb	0.0075	0.0690
Ia-Ic-BL	0.4416	0.0029
Ia-Ib/IIb	0.0004	0.0008
Ia-CC	0.0001	0.0202
II-Ic	0.0944	0.6855
II-Ib	0.7992	0.0038
II-Ibc	0.0886	0.1209
II-IIb	0.6427	0.0964
II-Ic-BL	0.8178	0.0068
II-Ib/IIb	0.7849	0.0034
Ic-Ib	0.3380	0.0622
Ic-IIb	0.0568	0.0439
Ic-Ic-BL	0.6309	0.0054
Ic-Ib/IIb	0.0537	0.0400
Ib-IIb	0.5754	0.6524
Ib-Ic-BL	0.6546	0.2813
IIb-Ic-BL	0.6342	0.1912

role between these types, and that other factors (e.g. progenitor mass) could be more important.

On the other hand, the radial distributions of different SNe types (see section 5.2) have been used as a proxy of environmental metallicity. If central regions of galaxies have higher metallicity, from distance distributions one can argue that the progenitors of SNe Ibc, being more centered, should be metal-rich than those producing other SNe types. This argument is consistent with the models claiming that SNe Ibc progenitors are massive stars whose envelopes have been stripped by stellar winds driven by metallicity prior to explosion (Puls et al. 1996; Kudritzki & Puls 2000; Mokiem et al. 2007). Since stars in higher metallicity environments suffer from stronger driven winds, SNe Ibc progenitors lose more mass through these winds prior to explosion, compared to SNe II which are in average further and in lower metallicity environments. However, we showed in section 3.2 that a significant fraction of SN host galaxies (~30%) present a decreasing gradient towards the center which, once accounted for, would imply lower environmental metallicities for objects closer to the center in those galaxies.

These two findings together question the importance of metallicity as the relevant factor in determining the SN type and supports that at least a fraction of them could come from binary systems, both compatible with being at lower radial distances. This is also in agreement with Haberman et al. (2012) and Anderson et al. (2015) who found that SN Ibc are more centralized compared to SNe II in interacting galaxies, where metallicity gradients are flatter or not present, pointing that other effects are playing a role besides metallicity in determining the SN type.

6. Conclusions

We present an updated sample of 115 galaxies with mean redshift $z = 0.015$ observed with IFS by the CALIFA survey. These galaxies hosted 132 SNe (47 type II, 27 type Ib/c+IIb, 58 Ia) that were within the FoV covered by the instrument. The spa-

tially resolved spectroscopy used in this work has several advantages with respect to the most common approaches, namely multi-wavelength photometry and fiber or slit spectroscopy. Indeed, IFS allows to obtain 2D maps of the most important parameters from both the stellar populations and the ionized gas emission. Following our previous work on the role of the local star-formation in determining the SN type, presented in Paper I, here we have focussed on the study and comparison of environmental metallicity for the various SN types. The relevance of this study is due to the influence of the SN progenitors metallicity on the supernova explosion and possible implications in high redshift supernova studies and determination of cosmological parameters with SN. Our main goals were: 1) unveil possible relations between the host metallicity at the SN location and the properties of the supernova or their progenitors; 2) identify systematic errors of the various proxies commonly used to infer the host metallicity at SN locations or the metallicity of the SN progenitors; and 3) estimate the accuracy in the determination of the local metallicity of the various proxies in high redshift supernova studies. To achieve a better comparison between galaxies, the radial dependence of galaxy properties was studied in units of the galaxy disk effective radius. We determined the galaxy disk effective radius by fitting a pure exponential function to their brightness profile and calculated the metallicity gradients for all galaxies. Different proxies to estimate the local metallicity were used, which allowed to search for differences among SN types. It also allowed to compare different proxies and to study their accuracy. Our main findings are summarized below.

- The gas-phase average metallicity at SN location show significant differences of ~ 0.04 dex between SN Ia and SN II, while the mass-weighted stellar metallicity at the SN location shows no significant difference between the three main SN groups.
- The total gas-phase metallicity distributions are undistinguishable among the SN groups (centered around 8.49 dex), while the total stellar metallicity distribution for SNe Ia is slightly shifted to higher values than SN II ($\langle Z_{Ia} \rangle - \langle Z_{II} \rangle = 0.015$).
- The difference between the local and the total metallicities are on average also small, and being significant only for SN Ia (0.03 dex). This is likely the result of the sample being biased toward galaxies with high masses; most galaxies have $\log(M/M_{\odot}) > 10.3$ dex.
- Several proxies of the local metallicity were studied. The most accurate proxies are those using the galaxy metallicity gradient plus the SN galactocentric distance and the metallicity of the closest HII region from the SN.
- The total galaxy metallicity is also a good proxy of the local metallicity for CC SNe, although we find a significant shift of ~ 0.03 dex for SNe Ia. We also find that weak AGNs that cannot be seen in the total spectrum may only weakly bias the metallicity estimate from the galaxy integrated spectrum by 0.03-0.04 dex. These results are encouraging for high-redshift studies as it allows the local metallicity to be estimated, although possible evolution of the metallicity gradient in galaxies with redshift may render this proxy less accurate.
- On the other hand we find that the central metallicity, with and without correction for the characteristic metallicity gradient, is the least accurate proxy, showing significant differences for both gas-phase and stellar metallicity. This can be due to the fact that about 30% of the galaxies show metallicity decrease toward the center, with further 10% showing just flattening.

- The local metallicity at the SN positions is not significantly different from the mean galaxy metallicity at the galactocentric distance of the SN. This argues against that certain SN type may prefer to explode in environments with specific metallicity.
- When the galaxy masses of our sample are combined with those from the literature it becomes clear that the targeted SN searches are biased toward high-mass galaxies. The average bias is $\log(M/M_{\odot}) = 0.8$.
- By extending our SN sample with published measurements of the metallicity at the vicinity of the SN, we studied the metallicity distributions for all SN subtypes split into SN discovered in targeted and untargeted searches. We confirm the known fact that there is bias toward high metallicity in the targeted searches.
- For the SN discovered in targeted searches, for which our sample is representative, we find that SN Ia and Ic have the highest metallicity than the other SN types. The difference are however small and in most cases statistically insignificant.
- In the untargeted searches SN Ia, Ic and II have higher metallicity comparing to the other SN types. Thus, it appears that SN Ib/Iib have significantly different local metallicities relative to SN Ic.
- Studying the evolution of the ratios between pairs of subtypes as a function of the metallicity, we found that the ratio of Ibc/II decreases with metallicity, and this is driven by SN Ib being at significantly lower metallicities. This gives support to the picture of SN Ib resulting from binary progenitors and (at least some) SN Ic resulting from single stars being stripped of their outer H and He layers by strong metallicity driven winds.

The CALIFA Survey has proven the use of Integral Field Spectroscopy as a powerful tool for SN environmental studies, in addition to the main aims of the survey which were the study of galaxy formation and evolution. The Sydney-AAO Multi-object Integral-field spectrograph (SAMI Croom et al. 2012) and the Mapping Nearby Galaxies at APO (MaNGA, (Bundy et al. 2015)) are the current largest IFS surveys and will increase the statistics by a factor ~ 5 to 20. However, they both lack of high spatial resolution which would be needed to get rid of the systematics effects studied in this work. Kuncarayakti et al. (2013a,b, 2015) performed a similar study than the one presented here and in Paper I, but studying the SN parent stellar clusters with resolutions around ~ 60 pc. Although this high resolution allows to properly distinguish among stellar clusters, the small field of view does not allow comparisons between local and other estimations of galaxy parameters across the galaxy. The advent of the new generation of instruments, such as the Multi-Unit Spectroscopic Explorer (MUSE) Integral Field Unit recently mounted to the 8m VLT UT4 (Bacon et al. 2010), would provide the required high spatial resolution together with larger field of view, joining the two requirements (See Sánchez et al. 2015; Galbany et al. 2016a; Anderson et al. 2015). This and other CALIFA studies will be improved with such a combination of these two factors.

Acknowledgements. We acknowledge the A&A editor, Rubina Kotak, for her timely and pertinent comments on preliminary versions of this manuscript. We acknowledge Joseph P. Anderson and Hanindy Kuncarayakti for fruitful discussions on SN environments (among many other topics). This work was partly funded by FCT with the research grant PTDC/CTE-AST/112582/2009. Support for LG is partially provided by FCT, by CONICYT through FONDECYT grant 3140566, and from the Ministry of Economy, Development, and Tourism's Millennium Science Initiative through grant IC12009, awarded to The Millennium Institute of Astrophysics (MAS). V.S. acknowledges financial support from

Fundação para a Ciência e a Tecnologia (FCT) under program Ciência 2008. CJW acknowledges support through the Marie Curie Career Integration Grant 303912. This study makes use of the data provided by the Calar Alto Legacy Integral Field Area (CALIFA) survey (<http://www.caha.es/CALIFA/>). CALIFA is the first legacy survey being performed at Calar Alto. The CALIFA collaboration would like to thank the IAA-CSIC and MPIA-MPG as major partners of the observatory, and CAHA itself, for the unique access to telescope time and support in manpower and infrastructures. The CALIFA collaboration thanks also the CAHA staff for the dedication to this project. Based on observations collected at the Centro Astronómico Hispano Alemán (CAHA) at Calar Alto, operated jointly by the Max-Planck Institut für Astronomie and the Instituto de Astrofísica de Andalucía (CSIC). The STARLIGHT project is supported by the Brazilian agencies CNPq, CAPES and FAPESP and by the France-Brazil CAPES/Cofecub program. This research has made use of the Asiago Supernova Catalogue, the SIMBAD database, operated at CDS, Strasbourg, France, the NASA/IPAC Extragalactic Database (NED), which is operated by the Jet Propulsion Laboratory, California Institute of Technology, under contract with the National Aeronautics and Space Administration, IAU Circulars presented by the Central Bureau for Astronomical Telegrams, and data products from SDSS and SDSS-II surveys. We acknowledge the usage of the HyperLeda database (<http://leda.univ-lyon1.fr>).

References

- Aldering, G., Humphreys, R. M., & Richmond, M. 1994, *AJ*, 107, 662
- Alloin, D., Collin-Souffrin, S., Joly, M., & Vigroux, L. 1979, *A&A*, 78, 200
- Anderson, J. P., Covarrubias, R. A., James, P. A., Hamuy, M., & Haberman, S. M. 2010, *MNRAS*, 407, 2660
- Anderson, J. P., González-Gaitán, S., Hamuy, M., et al. 2014, *ApJ*, 786, 67
- Anderson, J. P., Haberman, S. M., & James, P. A. 2011, *MNRAS*, 416, 567
- Anderson, J. P., Haberman, S. M., James, P. A., & Hamuy, M. 2012, *MNRAS*, 424, 1372
- Anderson, J. P. & James, P. A. 2009, *MNRAS*, 399, 559
- Anderson, J. P., James, P. A., Haberman, S. M., Galbany, L., & Kuncarayakti, H. 2015, *PASA*, 32, 19
- Arcavi, I., Gal-Yam, A., Cenko, S. B., et al. 2012, *ApJ*, 756, L30
- Arcavi, I., Gal-Yam, A., Kasliwal, M. M., et al. 2010, *ApJ*, 721, 777
- Arnett, W. D., Bahcall, J. N., Kirshner, R. P., & Woosley, S. E. 1989, *ARA&A*, 27, 629
- Bacon, R., Accardo, M., Adjali, L., et al. 2010, in *Society of Photo-Optical Instrumentation Engineers (SPIE) Conference Series*, Vol. 7735, Society of Photo-Optical Instrumentation Engineers (SPIE) Conference Series, 8
- Baldwin, J. A., Phillips, M. M., & Terlevich, R. 1981, *PASP*, 93, 5
- Bartunov, O. S., Makarova, I. N., & Tsvetkov, D. I. 1992, *A&A*, 264, 428
- Becker, S. A. & Iben, Jr., I. 1980, *ApJ*, 237, 111
- Bell, E. F., McIntosh, D. H., Katz, N., & Weinberg, M. D. 2003, *ApJS*, 149, 289
- Bersten, M. C., Benvenuto, O. G., Folatelli, G., et al. 2014, *AJ*, 148, 68
- Bethe, H. A., Brown, G. E., Applegate, J., & Lattimer, J. M. 1979, *Nuclear Physics A*, 324, 487
- Boissier, S. & Prantzos, N. 2009, *A&A*, 503, 137
- Bravo, E., Domínguez, I., Badenes, C., Piersanti, L., & Straniero, O. 2010, *ApJ*, 711, L66
- Bresolin, F., Gieren, W., Kudritzki, R.-P., et al. 2009, *ApJ*, 700, 309
- Bruzual, G. 2007, in *Astronomical Society of the Pacific Conference Series*, Vol. 374, *From Stars to Galaxies: Building the Pieces to Build Up the Universe*, ed. A. Vallenari, R. Tantalo, L. Portinari, & A. Moretti, 303
- Bundy, K., Bershad, M. A., Law, D. R., et al. 2015, *ApJ*, 798, 7
- Cappellari, M. & Copin, Y. 2003, *MNRAS*, 342, 345
- Childress, M., Aldering, G., Antilogus, P., et al. 2013, *ApJ*, 770, 107
- Cid Fernandes, R., Mateus, A., Sodré, L., Stasińska, G., & Gomes, J. M. 2005, *MNRAS*, 358, 363
- Claeys, J. S. W., de Mink, S. E., Pols, O. R., Eldridge, J. J., & Baes, M. 2011, *A&A*, 528, A131
- Croom, S. M., Lawrence, J. S., Bland-Hawthorn, J., et al. 2012, *MNRAS*, 421, 872
- Crowther, P. A. 2007, *ARA&A*, 45, 177
- de Vaucouleurs, G. 1948, *Annales d'Astrophysique*, 11, 247
- Dessart, L., Hillier, D. J., Livne, E., et al. 2011, *MNRAS*, 414, 2985
- Diaz, A. I. 1989, in *Evolutionary Phenomena in Galaxies*, ed. J. E. Beckman & B. E. J. Pagel, 377–397
- Diehl, S. & Statler, T. S. 2006, *MNRAS*, 368, 497
- Domínguez, I., Chieffi, A., Limongi, M., & Straniero, O. 1999, *ApJ*, 524, 226
- Eldridge, J. J., Fraser, M., Maund, J. R., & Smartt, S. J. 2015, *MNRAS*, 446, 2689
- Elias-Rosa, N., Van Dyk, S. D., Li, W., et al. 2011, *ApJ*, 742, 6
- Faran, T., Poznanski, D., Filippenko, A. V., et al. 2014, *MNRAS*, 445, 554
- Fathi, K., Beckman, J. E., Zurita, A., et al. 2007, *A&A*, 466, 905

- Folatelli, G., Bersten, M. C., Benvenuto, O. G., et al. 2014, *ApJ*, 793, L22
- Frey, L. H., Fryer, C. L., & Young, P. A. 2013, *ApJ*, 773, L7
- Fryer, C. L., Mazzali, P. A., Prochaska, J., et al. 2007, *PASP*, 119, 1211
- Gal-Yam, A. & Leonard, D. C. 2009, *Nature*, 458, 865
- Galbany, L., Anderson, J. P., Rosales-Ortega, F. F., et al. 2016a, *MNRAS*, 455, 4087
- Galbany, L., Hamuy, M., Phillips, M. M., et al. 2016b, *AJ*, 151, 33
- Galbany, L., Miquel, R., Östman, L., et al. 2012, *ApJ*, 755, 125
- Galbany, L., Stanishev, V., Mourão, A. M., et al. 2014, *A&A*, 572, A38
- García-Benito, R., Zibetti, S., Sánchez, S. F., et al. 2015, *A&A*, 576, A135
- Garnett, D. R., Shields, G. A., Skillman, E. D., Sagan, S. P., & Dufour, R. J. 1997, *ApJ*, 489, 63
- Gaskell, C. M., Cappellaro, E., Dinerstein, H. L., et al. 1986, *ApJ*, 306, L77
- Georgy, C., Meynet, G., Walder, R., Folini, D., & Maeder, A. 2009, *A&A*, 502, 611
- Gomes, J. M., Papaderos, P., Vílchez, J. M., et al. 2015, *ArXiv e-prints*
- González Delgado, R. M., Cid Fernandes, R., García-Benito, R., et al. 2014, *ApJ*, 791, L16
- González Delgado, R. M., García-Benito, R., Pérez, E., et al. 2015, *A&A*, 581, A103
- Graham, A. W., Driver, S. P., Petrosian, V., et al. 2005, *AJ*, 130, 1535
- Habergham, S. M., Anderson, J. P., James, P. A., & Lyman, J. D. 2014, *MNRAS*, 441, 2230
- Habergham, S. M., James, P. A., & Anderson, J. P. 2012, *MNRAS*, 424, 2841
- Hakobyan, A. A., Mamon, G. A., Petrosian, A. R., Kunth, D., & Turatto, M. 2009, *A&A*, 508, 1259
- Heger, A., Fryer, C. L., Woosley, S. E., Langer, N., & Hartmann, D. H. 2003, *ApJ*, 591, 288
- Henry, R. B. C. & Worthey, G. 1999, *PASP*, 111, 919
- Hillebrandt, W., Hoefflich, P., Weiss, A., & Truran, J. W. 1987, *Nature*, 327, 597
- Hoyle, F. & Fowler, W. A. 1960, *ApJ*, 132, 565
- Husemann, B., Jahnke, K., Sánchez, S. F., et al. 2013, *A&A*, 549, A87
- Iglesias-Páramo, J., Vílchez, J. M., Galbany, L., et al. 2013, *A&A*, 553, L7
- Inserra, C., Pastorello, A., Turatto, M., et al. 2013, *A&A*, 555, A142
- Izotov, Y. I., Stasińska, G., Meynet, G., Guseva, N. G., & Thuan, T. X. 2006, *A&A*, 448, 955
- Kehrig, C., Monreal-Ibero, A., Papaderos, P., et al. 2012, *A&A*, 540, A11
- Kelly, P. L., Hicken, M., Burke, D. L., Mandel, K. S., & Kirshner, R. P. 2010, *ApJ*, 715, 743
- Kelly, P. L. & Kirshner, R. P. 2012, *ApJ*, 759, 107
- Kewley, L. J., Dopita, M. A., Sutherland, R. S., Heisler, C. A., & Trevena, J. 2001, *ApJ*, 556, 121
- Kewley, L. J. & Ellison, S. L. 2008, *ApJ*, 681, 1183
- Kudritzki, R.-P. & Puls, J. 2000, *ARA&A*, 38, 613
- Kuncharayakti, H., Aldering, G., Anderson, J. P., et al. 2015, *Publication of Korean Astronomical Society*, 30, 139
- Kuncharayakti, H., Doi, M., Aldering, G., et al. 2013a, *AJ*, 146, 30
- Kuncharayakti, H., Doi, M., Aldering, G., et al. 2013b, *AJ*, 146, 31
- Leloudas, G., Gallazzi, A., Sollerman, J., et al. 2011, *A&A*, 530, A95
- Levesque, E. M., Soderberg, A. M., Foley, R. J., et al. 2010, *ApJ*, 709, L26
- Liu, Y.-Q., Modjaz, M., Bianco, F. B., & Graur, O. 2015, *ArXiv e-prints*
- Maoz, D., Sharon, K., & Gal-Yam, A. 2010, *ApJ*, 722, 1879
- Marino, R. A., Gil de Paz, A., Sánchez, S. F., et al. 2016, *A&A*, 585, A47
- Marino, R. A., Rosales-Ortega, F. F., Sánchez, S. F., et al. 2013, *A&A*, 559, A114
- Mast, D., Rosales-Ortega, F. F., Sánchez, S. F., et al. 2014, *A&A*, 561, A129
- Maund, J. R., Fraser, M., Ergon, M., et al. 2011, *ApJ*, 739, L37
- Maund, J. R., Smartt, S. J., Kudritzki, R. P., Podsiadlowski, P., & Gilmore, G. F. 2004, *Nature*, 427, 129
- McCully, C., Jha, S. W., Foley, R. J., et al. 2014, *Nature*, 512, 54
- Milisavljevic, D., Margutti, R., Soderberg, A. M., et al. 2013, *ApJ*, 767, 71
- Modjaz, M., Kewley, L., Bloom, J. S., et al. 2011, *ApJ*, 731, L4
- Modjaz, M., Kewley, L., Kirshner, R. P., et al. 2008, *AJ*, 135, 1136
- Mokiem, M. R., de Koter, A., Vink, J. S., et al. 2007, *A&A*, 473, 603
- Moreno-Raya, M. E., Mollá, M., López-Sánchez, Á. R., et al. 2016, *ApJ*, 818, L19
- Moustakas, J., Kennicutt, Jr., R. C., Tremonti, C. A., et al. 2010, *ApJS*, 190, 233
- Neill, J. D., Sullivan, M., Howell, D. A., et al. 2009, *ApJ*, 707, 1449
- Niino, Y., Nagamine, K., & Zhang, B. 2015, *MNRAS*, 449, 2706
- Nomoto, K., Iwamoto, K., Suzuki, T., et al. 1996, in *IAU Symposium*, Vol. 165, *Compact Stars in Binaries*, ed. J. van Paradijs, E. P. J. van den Heuvel, & E. Kuulkers, 119
- Pan, Y.-C., Sullivan, M., Maguire, K., et al. 2014, *MNRAS*, 438, 1391
- Panter, B., Jimenez, R., Heavens, A. F., & Charlot, S. 2008, *MNRAS*, 391, 1117
- Papaderos, P., Gomes, J. M., Vílchez, J. M., et al. 2013, *A&A*, 555, L1
- Petrosian, A., Navasardyan, H., Cappellaro, E., et al. 2005, *AJ*, 129, 1369
- Pettini, M. & Pagel, B. E. J. 2004, *MNRAS*, 348, L59
- Pilyugin, L. S. & Mattsson, L. 2011, *MNRAS*, 412, 1145
- Pilyugin, L. S., Vílchez, J. M., & Thuan, T. X. 2010, *ApJ*, 720, 1738
- Podsiadlowski, P., Joss, P. C., & Hsu, J. J. L. 1992, *ApJ*, 391, 246
- Prantzos, N. & Boissier, S. 2003, *A&A*, 406, 259
- Prieto, J. L., Lee, J. C., Drake, A. J., et al. 2012, *ApJ*, 745, 70
- Prieto, J. L., Stanek, K. Z., & Beacom, J. F. 2008, *ApJ*, 673, 999
- Puls, J., Kudritzki, R.-P., Herrero, A., et al. 1996, *A&A*, 305, 171
- Rolleston, W. R. J., Smartt, S. J., Dufton, P. L., & Ryans, R. S. I. 2000, *A&A*, 363, 537
- Rosales-Ortega, F. F., Díaz, A. I., Kennicutt, R. C., & Sánchez, S. F. 2011, *MNRAS*, 415, 2439
- Sahu, D. K., Tanaka, M., Anupama, G. C., Gurugubelli, U. K., & Nomoto, K. 2009, *ApJ*, 697, 676
- Salpeter, E. E. 1955, *ApJ*, 121, 161
- Sana, H., de Mink, S. E., de Koter, A., et al. 2012, *Science*, 337, 444
- Sánchez, S. F., Kennicutt, R. C., Gil de Paz, A., et al. 2012a, *A&A*, 538, A8
- Sánchez, S. F., Pérez, E., Rosales-Ortega, F. F., et al. 2015, *A&A*, 574, A47
- Sánchez, S. F., Rosales-Ortega, F. F., Iglesias-Páramo, J., et al. 2014, *A&A*, 563, A49
- Sánchez, S. F., Rosales-Ortega, F. F., Jungwiert, B., et al. 2013, *A&A*, 554, A58
- Sánchez, S. F., Rosales-Ortega, F. F., Marino, R. A., et al. 2012b, *A&A*, 546, A2
- Sánchez-Menguiano, L., Sánchez, S. F., Pérez, I., et al. 2016, *ArXiv e-prints*
- Sanders, N. E., Soderberg, A. M., Gezari, S., et al. 2015, *ApJ*, 799, 208
- Sanders, N. E., Soderberg, A. M., Levesque, E. M., et al. 2012, *ApJ*, 758, 132
- Sersic, J. L. 1968, *Atlas de galaxias australes (Cordoba, Argentina: Observatorio Astronomico)*, 1968)
- Shao, X., Liang, Y. C., Dennefeld, M., et al. 2014, *ApJ*, 791, 57
- Singh, R., van de Ven, G., Jahnke, K., et al. 2013, *A&A*, 558, A43
- Smartt, S. J. 2015, *PASA*, 32, 16
- Smith, N., Chornock, R., Li, W., et al. 2008, *ApJ*, 686, 467
- Smith, N., Li, W., Filippenko, A. V., & Chornock, R. 2011, *MNRAS*, 412, 1522
- Stanishev, V., Rodrigues, M., Mourão, A., & Flores, H. 2012, *A&A*, 545, A58
- Stasińska, G. 2006, *A&A*, 454, L127
- Stoll, R., Prieto, J. L., Stanek, K. Z., & Pogge, R. W. 2013, *ApJ*, 773, 12
- Sullivan, M., Conley, A., Howell, D. A., et al. 2010, *MNRAS*, 406, 782
- Taddia, F., Sollerman, J., Fremling, C., et al. 2015, *A&A*, 580, A131
- Taddia, F., Sollerman, J., Razza, A., et al. 2013, *A&A*, 558, A143
- Thöne, C. C., Michałowski, M. J., Leloudas, G., et al. 2009, *ApJ*, 698, 1307
- Tomasella, L., Cappellaro, E., Fraser, M., et al. 2013, *MNRAS*, 434, 1636
- Tsvetkov, D. Y., Pavlyuk, N. N., & Bartunov, O. S. 2004, *Astronomy Letters*, 30, 729
- van den Bergh, S. 1997, *AJ*, 113, 197
- van Dyk, S. D. 1992, *AJ*, 103, 1788
- Van Dyk, S. D., Davidge, T. J., Elias-Rosa, N., et al. 2012, *AJ*, 143, 19
- Van Dyk, S. D., Li, W., & Filippenko, A. V. 2003, *PASP*, 115, 1
- Van Dyk, S. D., Zheng, W., Fox, O. D., et al. 2014, *AJ*, 147, 37
- Veilleux, S. & Osterbrock, D. E. 1987, *ApJS*, 63, 295
- Vila-Costas, M. B. & Edmunds, M. G. 1992, *MNRAS*, 259, 121
- Walcher, C. J., Wisotzki, L., Bekeraite, S., et al. 2014, *A&A*, 569, A1
- Yoachim, P., Roškar, R., & Debattista, V. P. 2010, *ApJ*, 716, L4
- Young, D. R., Smartt, S. J., Valentí, S., et al. 2010, *A&A*, 512, A70
- Zaritsky, D., Kennicutt, Jr., R. C., & Huchra, J. P. 1994, *ApJ*, 420, 87

- 1 Millennium Institute of Astrophysics, Santiago, Chile.
- 2 Departamento de Astronomía, Universidad de Chile, Casilla 36-D, Santiago, Chile.
- 3 CENTRA - Centro Multidisciplinar de Astrofísica and Departamento de Física, Instituto Superior Técnico, ULisboa, Av. Rovisco Pais 1, 1049-001 Lisbon, Portugal.
- 4 European Southern Observatory, Alonso de Cordova 3107 Casilla 19001 - Vitacura - Santiago, Chile.
- 5 GEPI, Observatoire de Paris, UMR 8111, CNRS, Université Paris Diderot, 5 place Jules Janssen, 92190 Meudon, France.
- 6 Leibniz-Institut für Astrophysik Potsdam (AIP), An der Sternwarte 16, D-14482 Potsdam, Germany
- 7 Instituto de Astronomía, Universidad Nacional Autónoma de México, A.P. 70-264, 04510, México, D.F.
- 8 Instituto de Astrofísica de Andalucía (CSIC), Glorieta de la Astronomía s/n, Aptdo. 3004, E18080-Granada, Spain.
- 9 Instituto de Cosmologia, Relatividade e Astrofísica - ICRA, Centro Brasileiro de Pesquisas Físicas, Rua Dr. Xavier Sigaud 150, CEP 22290-180, Rio de Janeiro, RJ, Brazil.
- 10 Department of Physics and Astronomy, University of Pittsburgh, Allen Hall, 3941 O'Hara St, Pittsburgh PA 15260, USA.
- 11 Kapteyn Astronomical Institute, University of Groningen, PO Box 800, NL-9700 AV Groningen, the Netherlands.
- 12 Department of Physics, Institute for Astronomy, ETH Zürich, CH-8093 Zürich, Switzerland
- 13 Departamento de Astrofísica y CC. de la Atmósfera, Facultad de CC. Físicas, Universidad Complutense de Madrid, Avda. Complutense s/n, 28040 Madrid, Spain.
- 14 Departamento de Investigación Básica, CIEMAT, Avda. Complutense 40, E-28040 Madrid, Spain.
- 15 Max-Planck-Institut für Astronomie / Königstuhl 17 D-69117 Heidelberg, Germany.

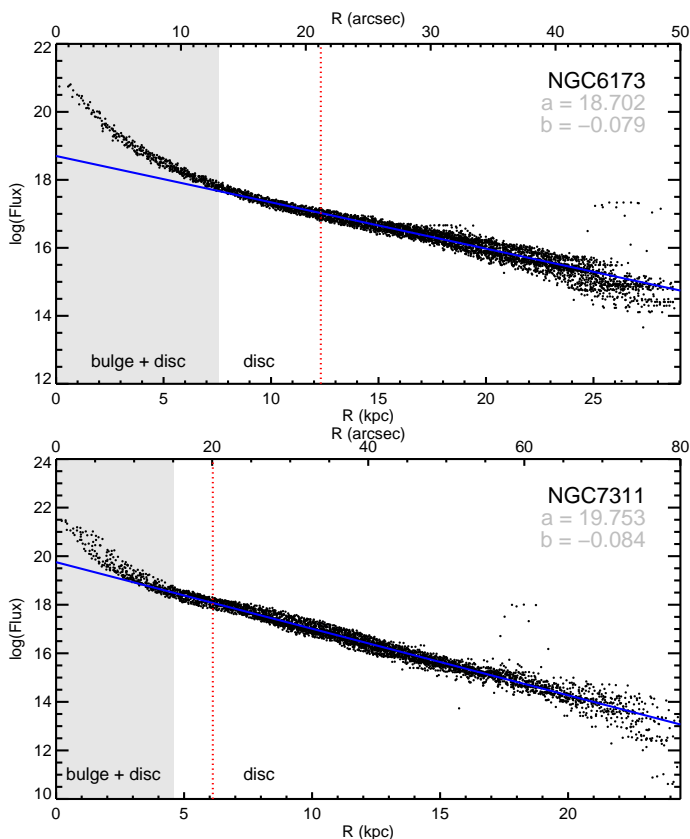


Fig. A.1. Two examples showing the determination of the disk effective radius. The grey shadow defines the region where the bulge contributes to the total surface brightness and it is excluded from the fit which is performed to the disk profile (solid blue line). The red vertical dotted line correspond to the disk effective radius, r_e , obtained from the Sérsic profile expression.

Appendix A: Disc effective radius (r_e)

The disk effective radius, r_e , is defined as the radius that contains half of the total integrated flux coming from the disk component. Its measurement permits to have a common ruler to properly compare the size of the galaxies and the derived quantities at a certain distance. To determine r_e we have performed a morphological decomposition based on the brightness profile. We integrated the flux under the r -band wavelength range in the spectrum of each spaxel, and then plotted the logarithm of these measurements against the deprojected GCD, as shown in Figure A.1 for NGC 6173 and NGC 7311. One can clearly see the contribution of both the central bulge and the disk to the total brightness of the galaxy. This mixture produces a combined surface brightness profile which can be described by an expression that depends on $r^{1/n}$ (de Vaucouleurs 1948; Sersic 1968; Graham et al. 2005; Galbany et al. 2012)

$$\log I(r) = \log I_0 - 1.6735 (r/r_e)^{1/n}. \quad (\text{A.1})$$

Depending on the size of the bulge, a different n is needed to properly describe the brightness profile. For example, elliptical galaxies that only have bulge are completely described by the de Vaucouleurs profile $r^{1/4}$ ($n = 4$), while pure disk galaxies match with a pure exponential profile ($n = 1$). In order to measure the effective radius of the disk component, we visually determined where the bulge vanishes, and fitted a pure exponential profile to the disk contribution, excluding the central regions dominated by the bulge. Finally, we obtained r_e as the distance at which the

logarithm of the flux is 1.6735 less than the central value of the fit to the disk profile. It is worth to note that fitting a line to these profiles is equivalent to obtain elliptical rings from the original image, since the inclination of the galaxies is taken into account in the deprojection.

We compared the values for the disk effective radii calculated in this work to the values obtained by other works in the CALIFA collaboration. We used two sets of measurements: (i) those measured with a growth curve photometry analysis presented in Walcher et al. (2014), and (ii) those measured in Sánchez et al. (2014), that used a similar procedure to the one presented here. For the galaxies in common (basically those from the CALIFA mother sample), we obtained similar values (within 10%) for almost all the galaxies. For six galaxies we obtained larger differences but, after repeating the analysis without those, the final results in terms of the common slope, do not change significantly when using Walcher et al. (2014) or Sánchez et al. (2014) values.

Appendix B: Characteristic metallicity gradient

In this appendix we present the distributions of slopes of the metallicity gradients for our SN host galaxy sample. The central decrease was excluded in the metallicity gradient fits, resulting in different ranges for each galaxy up to 2 disk effective radius. The mean metallicity gradient of all 104 galaxies is $-0.016 (\pm 0.013)$ dex kpc^{-1} with the uncertainty being the standard deviation of the distribution. When the distances are normalized to the disk effective radius r_e , the average gradient becomes $-0.074 (\pm 0.042)$ dex r_e^{-1} (using the O3N2 calibration from M13). The distribution of the normalized gradients is shown in Fig. B.1. Note that the relative scatter of the normalized gradients is smaller than in physical units. In addition, the scatter is fairly low, suggesting a characteristic radial gradient for the oxygen abundance in normalized units. This is in agreement with the results presented by Sánchez et al. (2012b), Sánchez et al. (2014) and Sánchez-Menguiano et al. (2016), who reported an average gradient of -0.1 dex r_e^{-1} using the PP04 calibration (we find -0.105 dex r_e^{-1} with that calibration).

The statistics of the distributions using the main calibrator and the comparison methods are presented in Table B.1. The mean values of the distributions of the metallicity gradients for P10 and P11 strong line methods are around -0.08 dex r_e^{-1} . Five galaxies (UGC 01087, UGC 04036, UGC 4107, NGC 6643, and NGC 3913) have no [O II] line measurement and no P10 abundance estimation can be computed, while IC 0307 and NGC 6166 have no [S II] lines measured and no P11 measurements can be performed. As expected, the distribution of metallicity gradients measured using N2 calibrator has lower values. This calibrator is not well defined in the high metallicity regime and the range of allowed values is narrower, thus flattening the measured gradients. We note that although not significant, SNe Ia host galaxies show flatter gradients than both CC SN hosts. Also noticeable is the narrower distribution of the O3N2 distribution.

Appendix C: The effect of AGNs on total spectra

The central spectra of about 29% of CC SN hosts, 59% of the star-forming, and all passive SN Ia hosts (see section 4.2.1) in our sample indicate the presence of AGN accord-

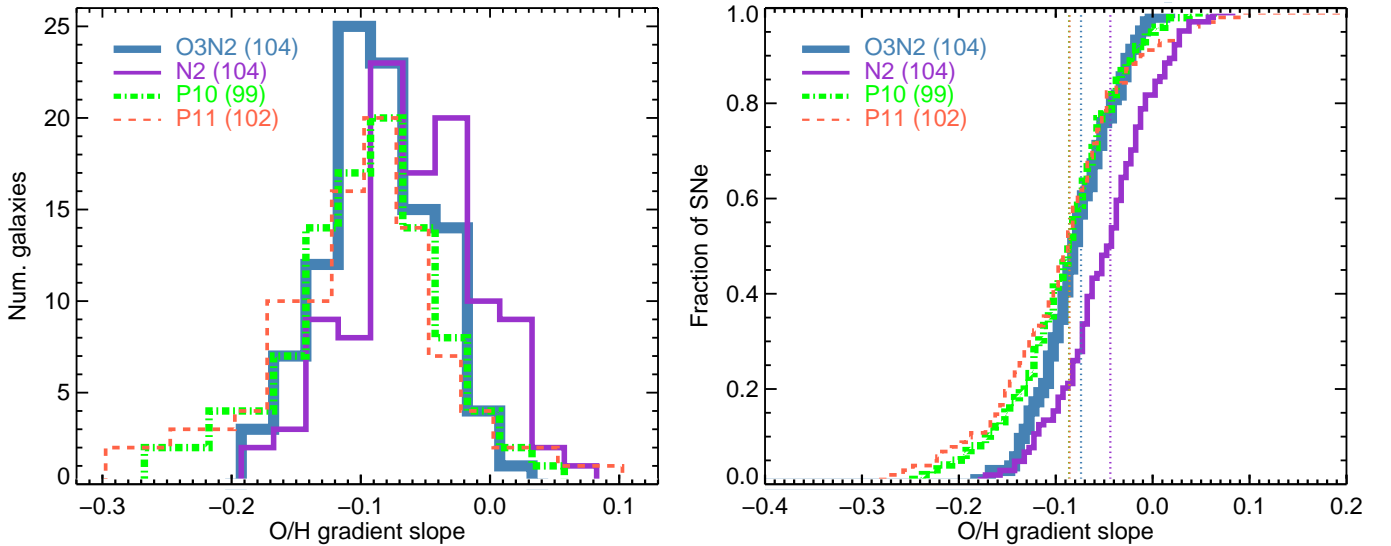


Fig. B.1. Distribution of metallicity gradients using O3N2 (blue), N2 (purple), P10 (green), and P11 (red) methods. All fits were done considering the errors in each spaxel measurement.

Table B.1. Average values of the metallicity gradient slopes and the standard deviation of the distributions.

	O3N2		N2		P10		P11	
	#	avg.	#	avg.	#	avg.	#	avg.
All Galaxies	104	-0.074 (0.042)	104	-0.044 (0.052)	99	-0.086 (0.059)	102	-0.086 (0.087)
SN Ia hosts	46	-0.064 (0.041)	46	-0.046 (0.050)	43	-0.077 (0.064)	46	-0.077 (0.117)
SN Ibc hosts	27	-0.078 (0.040)	27	-0.040 (0.053)	25	-0.087 (0.050)	26	-0.094 (0.049)
SN II hosts	47	-0.087 (0.037)	47	-0.037 (0.052)	46	-0.091 (0.049)	47	-0.090 (0.050)

ing to the Kewley et al. (2001) criterion in the BPT diagram⁵ (Baldwin et al. 1981; Veilleux & Osterbrock 1987). The emission line measurements from the total spectra of most star-forming galaxies with AGN fall in the star-forming region of the BPT diagram. This indicates that the AGNs are not strong enough to affect significantly the total spectrum. The passive galaxies are exception because most of the emission comes from the center and when AGN is present, its emission may dominate the total emission line spectrum. For this reason the passive galaxies were not considered in the analysis of the effect of AGNs.

Even though the AGNs in our galaxy sample are not particularly strong, their presence can still affect the metallicity estimates and bias the results from the total spectra. To study this, for each cube two different extractions of the total spectrum were done. First, we just summed up the flux in all the spaxels with a S/N greater than 1.0. As an alternative, we did the same but excluding those central spaxels that fall in the AGN region of the so-called BPT diagnostic diagram. The first spectrum would correspond to the spectrum of a galaxy at high redshift or a small galaxy at lower redshift when the whole galaxy falls into the slit or the fiber of the spectrograph.

Figure C.1 shows gas-phase metallicity estimated from the total spectra with and without including the central spaxels falling in the AGN region. All values are close or above the diagonal, indicating that the metallicity measured from a spectrum including the AGN contribution is usually lower than the

measurement excluding it. In general, there is a good agreement between the measurements from the two total spectra for the CC SN hosts. However, for the SN Ia host galaxies the abundances are on average higher by 0.03–0.04 dex when the AGN contribution is removed. This difference raises a potential problem in the metallicity estimation from spectra of high redshift SN Ia hosts since the presence of a weak AGN contribution might be missed. Thus, the metallicity measured from total galaxy spectra should be considered as a lower limit with a systematic error of at least 0.03 dex. However, concerning the mean total gas-phase metallicity of the galaxies in our sample, the AGNs have little effect. When using the measurement with AGN contribution removed the mean metallicity of the SN Ia hosts becomes larger by only 0.012 dex and no change is observed for CC SN hosts.

Appendix D: Measured quantities

⁵ Kehrig et al. (2012), Singh et al. (2013) and Papaderos et al. (2013) using CALIFA data have shown that in some galaxies narrow line emission that falls in the AGN section of the BPT diagram, is not due to AGN activity but from old post-AGB stars.

Table D.1. Parameters of the CALIFA galaxies that hosted SNe outside the instrument field of view.

Galaxy	SN name	SN type	AGN	z	OH total	$\log(Z_m / Z_\odot)$	Mass [M_\odot]
NGC3184	1921C	I	-	0.001975	8.82	-0.02	10.30
NGC0477	2002jy	Ia	-	0.019600	8.65	-0.03	10.94
NGC2487	1975O	Ia	+	0.016148	8.71	-0.05	11.14
NGC2513	2010ja	Ia	+	0.015561	...	0.12	11.53
NGC3160	1997C	Ia	+	0.023083	...	-0.06	11.07
NGC4185	1982C	Ia	-	0.013022	8.73	0.02	11.01
NGC5485	1982W	Ia	+	0.006428	...	0.10	10.90
NGC5532	2007ao	Ia	+	0.024704	...	0.11	11.94
NGC5557	2013gn	Ia	+	0.010737	...	0.16	11.48
IC1151	1991M	Ia	-	0.007235	8.53	-0.38	10.02
NGC6027	2006ay	Ia	-	0.014834	8.64	-0.03	11.08
NGC6411	1999da	Ia	+	0.012695	...	0.04	11.15
NGC7549	2009nq	Ia	-	0.015799	8.74	-0.22	10.78
NGC7782	2003gl	Ia	+	0.017942	8.67	0.21	11.44
NGC3913	1979B	Ia	-	0.003182	8.73	-0.47	9.27
NGC0171	2009hf	IIP	+	0.013043	8.69	0.09	10.98
NGC0180	2001dj	IIpec	+	0.017616	8.81	0.02	11.12
NGC0309	2012dt	II	c	0.018886	8.82	0.05	11.19
NGC0941	2005ad	IIP	-	0.005364	8.58	-0.34	9.76
UGC10710	2000bs	IIP	-	0.027976	8.65	0.02	10.87
NGC1058	1969L	IIP	+	0.001728	8.68	-0.41	9.11
NGC3184	1937F	IIP	-	0.001975	8.82	-0.02	10.30
NGC3184	1921B	II	-	0.001975	8.82	-0.02	10.30
NGC0214	2006ep	Ib	+	0.015134	8.73	0.04	11.30
UGC04308	1962F	IIb	-	0.011895	8.69	-0.17	10.68
NGC6060	1997dd	IIb	-	0.014807	8.67	0.04	11.30
NGC0309	2008cx	IIb	c	0.018886	8.82	0.05	11.19
NGC0628	2002ap	Ic-bl	c	0.002192	8.69	-0.49	10.30

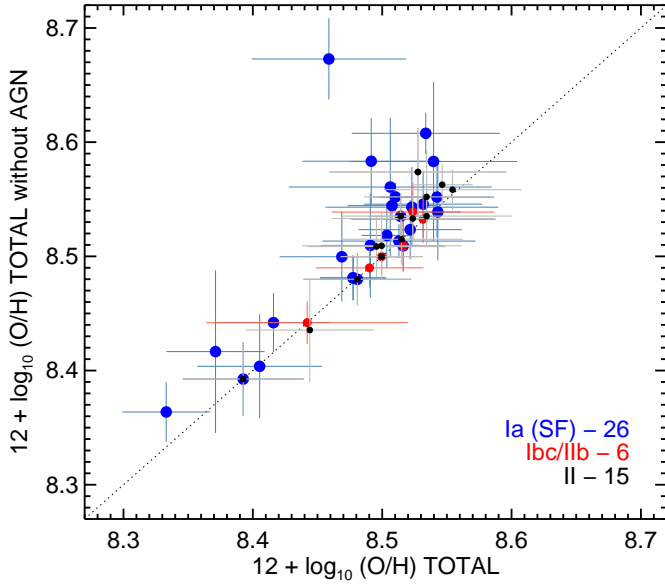
**Fig. C.1.** Comparison between the average oxygen abundance with and without the AGN contribution.

Table D.2. Type Ia SNe results.

Galaxy	SN name	SN type	AGN	r_e [kpc]	dep-GCD [kpc]	Mass [M_\odot]	$12 + \log(O/H)$			$\log(Z_m/Z_\odot)$	
							Gradient [dex r_e^{-1}]	Local	Total	Local	Total
NGC 2565	1960M	I	+	4.8	9.4	11.11	-0.082	8.46	8.48	0.04	-0.04
NGC 7319	1971P	I	+	11.1	14.7	11.32	-0.067	...	8.37	...	-0.04
NGC 5668	1954B	Ia	+	3.4	2.2	11.38	-0.108	8.42	8.39	-0.07	-0.10
NGC 3913	1963J	Ia	-	1.4	0.9	9.27	-0.071	8.54	8.53	...	-0.06
NGC 3811	1969C	Ia	-	3.9	2.5	10.79	-0.118	8.54	8.51	0.09	0.18
NGC 7619	1970J	Ia	+	5.3	10.5	11.52	-0.056	-0.40
NGC 4874	1981G	Ia	+	11.9	9.2	11.69	0.013	0.01	0.10
NGC 1667	1986N	Ia	+	5.6	6.8	11.29	-0.078	8.56	8.51	...	-0.23
NGC 3687	1989A	Ia	+	3.1	4.7	10.43	-0.084	8.47	8.51	...	0.05
NGC 5378	1991ak	Ia	+	6.6	8.1	10.78	-0.037	8.50	8.47	-0.45	-0.51
NGC 0932	1992bf	Ia	+	7.1	4.1	11.26	-0.018	8.42	8.51	0.12	-0.26
UGC 04036	1995E	Ia	+	9.5	5.4	10.94	-0.089	8.57	8.50	0.15	-0.07
NGC 5157	1995L	Ia	+	10.7	9.4	11.33	-0.003	8.54	8.49	0.16	-0.05
NGC 5557	1996aa	Ia	+	4.8	1.4	11.48	-0.114	-0.07
NGC 3982	1998aq	Ia	+	1.2	1.6	10.82	-0.068	8.56	8.51	-0.08	0.22
UGC 00139	1998dk	Ia	-	5.5	1.8	10.18	-0.136	8.52	8.40	0.18	0.10
UGC 01087	1999dk	Ia	c	5.8	8.2	10.65	-0.135	8.47	8.49	...	-0.08
NGC 0495	1999ej	Ia	+	4.1	7.5	10.84	-0.019	0.22	-0.02
NGC 2623	1999gd	Ia	+	4.2	6.9	10.92	0.018	8.52	8.49	0.22	0.11
UGC 04195	2000ce	Ia	-	6.4	8.0	10.85	-0.091	8.54	8.50	...	-0.06
NGC 0523	2001en	Ia	c	7.4	8.3	10.78	-0.090	8.47	8.45	...	-0.13
UGC 05129	2001fe	Ia	+	3.8	3.6	10.63	-0.075	8.58	8.52	...	-0.41
2MFGC 13321	2002aw	Ia	+	4.8	3.2	10.76	-0.053	8.48	8.54	...	-0.06
NGC 7253	2002jg	Ia	-	13.1	7.3	10.80	0.003	8.54	8.55	0.18	0.05
MCG -02-02-086	2003ic	Ia	+	18.4	10.9	11.91	-0.130	-0.11	-0.31
UGC 00005	2003lq	Ia	+	11.0	19.2	11.27	-0.101	...	8.51	0.13	0.07
UGC 10097	2004di	Ia	+	11.4	22.0	11.32	-0.035	...	8.46	0.11	0.06
NGC 1060	2004fd	Ia	+	7.0	2.1	11.86	-0.023	-0.46	-0.26
MCG -01-09-006	2005eq	Ia	c	10.7	21.7	11.24	-0.101	8.47	8.49	-0.25	-0.19
NGC 7311	2005kc	Ia	+	6.1	5.9	10.77	-0.089	8.58	8.52	-0.03	0.04
UGC 04468	2006bb	Ia	+	20.2	14.8	11.34	0.030	-0.02	0.11
NGC 5587	2006dy	Ia	+	3.7	6.0	10.58	-0.024	8.53	8.53	0.16	-0.07
CGCG 207-042	2006te	Ia	-	6.5	6.3	10.50	-0.075	8.56	8.46	...	-0.41
NGC 0105	2007A	Ia	+	4.2	3.6	10.88	-0.106	8.60	8.48	...	-0.49
UGC 04008	2007R	Ia	c	10.4	3.0	11.37	-0.026	8.56	8.55	...	-0.49
NGC 2577	2007ax	Ia	+	3.3	1.5	10.88	-0.063	-0.51
UGC 04455	2007bd	Ia	+	8.2	6.3	11.15	-0.053	8.58	8.54	-0.53	-0.65
NGC 7469	2008ec	Ia	+	3.7	5.2	11.36	-0.001	8.48	8.42	0.21	0.18
NGC 6166	2009eu	Ia	+	11.5	20.9	11.37	-0.008	0.15	0.08
NGC 5525	2009gt	Ia	-	12.2	28.1	11.33	-0.112	...	8.50	...	-0.33
NGC 6146	2009fl	Ia	+	8.8	7.7	11.62	-0.049	-0.62	-0.43
NGC 6173	2009fv	Ia	+	12.3	5.8	11.86	-0.011	-0.01	0.14
NGC 7364	2009fk	Ia	c	4.9	2.6	10.80	-0.018	8.58	8.57	0.02	0.04
UGC 11975	2011fs	Ia	-	5.2	16.8	10.81	-0.045	...	8.56	...	0.05
NGC 7364	2011im	Ia	c	4.9	9.7	10.80	-0.018	8.57	8.57	...	0.16
NGC 5421	2012T	Ia	c	6.8	3.0	11.33	-0.049	8.52	8.51	-0.09	0.08
NGC 5611	2012ei	Ia	+	2.2	2.1	10.38	-0.076	0.09	0.09
UGC 08250	2013T	Ia	-	7.3	12.6	10.31	-0.064	8.39	8.39	...	-0.16
NGC 7321	2013di	Ia	+	7.6	12.2	10.73	-0.103	8.53	8.52	0.12	0.04
NGC 2554	2013gq	Ia	+	6.0	2.6	11.39	-0.009	8.50	8.41	...	0.03
NGC 6166	PS15aot	Ia	+	11.5	5.4	11.37	-0.008	0.14
NGC 0938	2015ab	Ia	+	5.1	3.8	11.12	-0.013	8.43	8.34	...	-0.33
UGC 03151	1995bd	Iapec	+	6.0	7.1	11.06	-0.011	8.59	8.53	0.16	0.07
NGC 0105	1997cw	Iapec	+	4.2	3.5	10.88	-0.106	8.56	8.48	0.03	0.15
NGC 2595	1999aa	Iapec	-	9.1	8.2	11.18	-0.038	8.45	8.51	0.19	0.17
NGC 6063	1999ac	Iapec	c	5.1	7.7	10.39	-0.120	...	8.48	-0.11	0.13
NGC 0976	1999dq	Iapec	+	7.5	2.6	11.15	-0.030	8.62	8.54	0.02	0.07
NGC 2691	2011hr	Iapec	c	5.7	2.1	10.68	-0.055	8.56	8.49	0.16	0.04

Table D.3. Type II SNe results.

Galaxy	SN	SN type	AGN	r_{eff}	dep-GCD	Mass	12 + log (O/H)			Z_m	
							grad	local	total	local	total
NGC 3811	1971K	II	–	3.9	7.6	10.79	–0.118	8.50	8.51	–0.16	–0.40
NGC 2565	1992I	II	+	4.8	13.3	11.11	–0.082	8.60	8.48	–0.01	0.10
NGC 3057	1997cx	II	–	3.6	1.7	9.51	–0.095	8.33	8.28	0.09	–0.06
NGC 2916	1998ar	II	+	7.8	10.8	11.07	–0.135	...	8.50	...	–0.39
UGC 03555	1999ed	II	–	4.7	6.4	11.12	–0.134	8.50	8.46	0.09	0.10
NGC 0309	1999ge	II	c	12.0	6.8	11.19	–0.087	8.70	8.60	–0.03	0.04
UGC 05520	2000L	II	–	5.3	6.6	10.03	–0.180	8.33	8.37	0.15	0.06
UGC 00005	2000da	II	+	11.0	7.7	11.27	–0.101	8.61	8.51	0.05	–0.21
MCG -01-10-019	2001H	II	–	8.8	3.2	10.40	–0.123	8.56	8.46	0.04	0.06
NGC 2604	2002ce	II	–	3.4	3.0	10.05	–0.092	8.33	8.38	0.07	0.22
NGC 7771	2003hg	II	–	3.7	3.6	11.28	–0.055	8.61	8.50	–0.40	0.01
UGC 00148	2003ld	II	–	7.5	2.5	10.24	–0.040	8.43	8.40	–0.67	–0.63
NGC 5668	2004G	II	+	3.4	5.6	11.38	–0.108	...	8.39	–0.04	0.10
NGC 5980	2004ci	II	c	5.5	6.1	11.12	–0.120	8.56	8.53	–0.47	–0.09
NGC 6786	2004ed	II	–	5.2	5.3	11.54	–0.089	8.55	8.55	0.10	0.10
NGC 5056	2005au	II	c	6.6	8.1	11.00	–0.122	8.43	8.45	0.14	0.13
NGC 5682	2005ci	II	–	3.4	1.9	9.54	–0.083	8.32	8.35	...	0.06
NGC 5630	2005dp	II	–	3.3	4.8	9.89	–0.057	8.35	8.32	...	0.03
UGC 04132	2005en	II	–	8.1	6.8	11.34	–0.104	8.46	8.51	0.07	0.13
NGC 0774	2006ee	II	+	7.8	4.8	10.42	–0.161	8.50	8.44	0.04	0.05
NGC 5888	2007Q	II	+	11.2	12.6	11.41	–0.053	8.56	8.53	...	0.22
NGC 6643	2008ij	II	–	4.5	3.0	10.46	–0.101	8.53	8.52	0.20	0.10
NGC 5888	2010fv	II	+	11.2	9.1	11.41	–0.053	8.68	8.53	0.13	–0.08
NGC 1056	2011aq	II	c	2.6	0.7	10.57	–0.075	8.49	8.44	–0.38	–0.15
NGC 5425	2011ck	II	–	2.7	2.8	9.83	–0.113	8.42	8.38	0.07	0.17
NGC 5732	ASASSN-14fj	II	–	4.8	8.3	10.33	–0.162	8.36	8.47	–0.24	0.04
NGC 5406	PSN J14002117 +3854517	II	+	7.1	2.0	11.22	–0.072	8.50	8.54	...	0.20
IC 0758	1999bg	IIP	–	1.8	3.4	9.32	–0.049	8.35	8.43	0.21	–0.02
NGC 1637	1999em	IIP	c	2.5	1.1	9.74	–0.020	8.64	8.58	0.22	0.08
NGC 3184	1999gi	IIP	–	2.2	2.5	10.30	–0.057	8.63	8.60	...	–0.02
NGC 2347	2001ee	IIP	+	4.6	6.2	11.19	–0.093	8.52	8.51	0.05	0.17
NGC 5772	2002ee	IIP	+	7.5	12.9	10.52	–0.069	8.44	8.52	0.17	0.03
NGC 0628	2003gd	IIP	c	3.2	7.3	10.29	–0.132	8.48	8.51	...	0.14
NGC 1093	2009ie	IIP	+	6.5	16.2	10.96	–0.074	8.49	8.50	0.05	0.20
UGC 09356	2011cj	IIP	–	2.4	2.6	9.88	–0.081	8.40	8.42	–0.10	0.01
NGC 0628	2013ej	IIP	c	3.2	7.4	10.29	–0.132	...	8.51	0.20	0.01
NGC 7691	2014az	IIP	–	8.2	7.8	10.50	–0.025	8.45	8.49	–0.16	–0.32
UGC 10123	2014cv	IIP	c	4.0	2.7	10.68	–0.044	8.53	8.50	–0.09	0.16
UGC 01635	2003G	IIn	c	6.1	2.8	10.42	–0.025	8.64	8.56	0.19	0.12
NGC 0214	2005db	IIn	+	7.1	5.6	11.30	–0.033	8.68	8.53	–0.08	0.06
NGC 2906	2005ip	IIn	+	3.2	4.0	10.91	–0.081	8.40	8.55	0.02	0.01
NGC 5630	2006am	IIn	–	3.3	2.7	9.89	–0.057	8.31	8.32	...	–0.00
NGC 4644	2007cm	IIn	+	4.2	8.4	10.84	–0.052	8.51	8.53	0.05	0.09
NGC 5829	2008B	IIn	–	6.3	9.0	10.33	–0.098	8.50	8.46	0.19	0.17
UGC 09842	2012as	IIn	c	11.0	20.1	10.90	–0.087	8.46	8.50	–0.40	–0.28
UGC 04132	2014ee	IIn	–	8.1	10.1	11.34	–0.104	8.47	8.51	...	–0.32
NGC 1058	1961V	IIPec	+	1.0	2.7	9.11	–0.072	8.23	8.50	0.15	0.16

Table D.4. Type Ibc/IIb SNe results.

Galaxy	SN	SN type	AGN	r_{eff}	dep-GCD	Mass	$12 + \log(O/H)$			$\log(Z_m/Z_\odot)$	
							grad	local	total	local	total
NGC 3655	2002ji	Ibc	c	1.8	3.0	10.74	-0.064	8.54	8.55	-0.49	-0.47
NGC 5714	2003dr	Ibc	-	4.8	7.8	10.26	-0.079	8.39	8.49	-0.03	-0.35
UGC 06517	2006lv	Ibc	-	3.0	2.6	10.04	-0.130	8.52	8.46	...	-0.11
UGC 02134	2011jf	Ibc	c	6.6	0.9	11.02	-0.028	8.58	8.52	...	-0.07
UGC 04107	1997ef	Ibc-pec	-	5.9	5.4	10.82	-0.096	8.50	8.52	-0.25	-0.24
NGC 5559	2001co	Ibc-pec	c	6.2	7.8	11.10	-0.088	8.56	8.48	0.16	-0.11
NGC 0991	1984L	Ib	+	3.8	4.3	9.63	-0.142	8.43	8.44	0.22	0.09
NGC 5480	1988L	Ib	-	3.1	1.9	10.34	-0.045	8.58	8.55	-0.26	0.01
NGC 0776	1999di	Ib	c	8.0	5.9	11.16	-0.076	8.67	8.59	0.19	0.06
NGC 2596	2003bp	Ib	-	8.7	9.2	11.16	-0.123	8.51	8.49	0.11	0.01
NGC 7364	2006lc	Ib	c	4.9	4.2	10.80	-0.018	8.57	8.57	0.09	-0.19
NGC 6186	2011gd	Ib	-	4.2	0.6	10.77	-0.039	8.60	8.58	0.04	0.09
UGC 05100	2002au	IIb	-	4.6	7.9	11.18	-0.058	8.50	8.50	0.19	0.11
IC 0307	2005em	IIb	c	11.7	12.1	11.34	-0.077	...	8.49	...	-0.20
NGC 5735	2006qp	IIb	+	5.7	9.3	10.75	-0.139	8.40	8.49	0.07	-0.05
NGC 6643	2008bo	IIb	-	4.5	3.7	10.46	-0.101	...	8.52	-0.03	0.02
NGC 1070	2008ie	IIb	+	6.2	8.7	11.13	0.020	8.63	8.52	0.05	-0.20
UGC 10331	2011jg	IIb	-	5.8	6.7	10.36	-0.072	8.39	8.37	...	-0.04
NGC 3310	1991N	Ic	c	1.5	0.6	10.13	-0.027	8.35	8.33	-0.07	0.03
MCG -01-54-016	2001ch	Ic	-	4.4	4.4	9.19	-0.065	8.12	8.24	...	0.10
NGC 4210	2002ho	Ic	+	4.3	3.5	10.59	-0.097	8.56	8.53	...	0.22
NGC 5000	2003el	Ic	c	6.2	6.6	11.08	-0.048	8.58	8.53	-0.02	-0.13
UGC 03555	2004ge	Ic	-	4.7	2.0	11.12	-0.134	8.58	8.46	0.22	0.14
NGC 4961	2005az	Ic	-	3.0	1.8	10.03	-0.104	8.49	8.44	0.16	0.17
UGC 04132	2005eo	Ic	-	8.1	9.9	11.34	-0.104	8.49	8.51	0.20	0.20
NGC 1058	2007gr	Ic	+	1.0	1.0	9.11	-0.072	8.54	8.50	...	-0.59
NGC 7321	2008gj	Ic	+	7.6	17.8	10.73	-0.103	8.39	8.52	...	0.02